LATENT HEATING PROFILES OVER THE AMAZON IN RELATION TO THE ATLANTIC WALKER CIRCULATION

A Thesis

by

EMILY ELIZABETH MONROE

Submitted to the Office of Graduate and Professional Studies of
Texas A&M University
in partial fulfillment of the requirements for the degree of

MASTER OF SCIENCE

Chair of Committee,	Courtney Schumacher
Committee Members,	Ping Chang
	Georgianne Moore
Head of Department,	Ping Yang

December 2016

Major Subject: Atmospheric Sciences

ABSTRACT

The western rising branch of the local Walker circulation over the Atlantic intensifies as a result of enhanced convection and the associated latent heat release over the greater Amazon region. Monthly measurements gathered from 16 years of Tropical Rainfall Measuring Mission (TRMM) precipitation radar (PR) data are used to construct a latent heating climatology, which is then compared to those generated by the Convective and Stratiform Heating (CSH), Spectral Latent Heating (SLH), and variational analysis algorithms, to determine methodological accuracy. Three-dimensional reflectivity measurements collected during the Green Ocean Amazon experiment (GOAmazon2014/5) by the Sistema de Proteção da Amazônia (SIPAM) S-band Doppler radar located in Manaus in the central Amazon are also used to calculate latent heating profiles, and are compared to local sounding budgets. While all of the methods show similar seasonal cycles of latent heating, there are notable differences in the magnitude and height of maximum heating. Years are then identified as having higher or lower heat release during the Amazon wet season in boreal spring. Sea-level pressure, sea surface temperature, and surface wind measurements over the equatorial Atlantic are analyzed to determine the relative effect of an enhanced rising branch of the Walker circulation using data from Modern-Era Retrospective analysis for Research and Applications version 2 (MERRA-2). Higher heating over the Amazon during the wet season generally strengthens the Walker circulation over the equatorial Atlantic during boreal spring and yields lower surface pressures, stronger easterlies, and a delayed cold tongue in the equatorial Atlantic during boreal summer. This work provides observational confirmation of a strong link between Amazonian heating and the Atlantic Walker circulation, which has implications for improving significant biases in global climate models over the Amazon and Atlantic and enhancing our understanding of

how Amazonian rainfall links to tropical climate variability.

TABLE OF CONTENTS

Page

LIST OF FIGURES

FIGURE Page

LIST OF TABLES

TABLE Page

1. INTRODUCTION AND MOTIVATION

The tropics are generally defined to be a latitudinal band between 20^{o}N and 20^{o}S. Due to the equatorial location, with Earth-sun geometry keeping some portion of the tropics directly underneath the sun's rays at any given time, there is an above-average amount of solar radiation received, and thus a surplus of energy and heat in the boundary layer. As a result, differences between surface and free tropospheric temperatures can be amplified in the equatorial regions. To maintain a global equilibrium and prevent surface temperatures in the tropics from continually rising, a redistribution of heat is necessary.

In the vertical, this transfer is driven primarily by convection, or the tendency of warm, moist air close to the surface to rise, with larger density differences between a parcel of air and its environment leading to a greater amount of lift. As the parcel rises, saturation is reached and water vapor condenses, resulting in cloud formation and development, which can then lead to precipitation. In no small part due to the high amount of radiation received and associated vertical motion, approximately two-thirds of global rainfall occurs in the tropics, and approximately 75% of the energy driving atmospheric circulation is due to the associated latent heat release (Kummerow et al., 2000).

1.1 Latent heat

Rain and its impact on the large-scale environment can be diagnosed in terms of latent heating. Latent heat is a direct result of the phase change of water in the atmosphere, with latent heat *release* from the water into its environment being associated with condensation, freezing, and deposition, and latent heat *absorption* by the water (and thus cooling of the environment) being associated with melting, evaporation, and sublimation. Therefore, as the water vapor in an air parcel condenses in the formation of clouds and precipitation, latent heat is released thereby enhancing the temperature difference between a rising

parcel of air and its environment and yielding positive buoyancy that can subsequently lead to further adiabatic cooling and condensation. This upward motion associated with the release of latent heat serves as the primary engine for the vertical motion and overall transport of energy from the surface to upper levels (Riehl and Malkus, 1957; Yanai et al., 1973; Simpson, 1992).

The Amazon experiences significant precipitation due to two main characteristics: its location near the equator, where rainfall is more likely to occur due to the amount of received radiation, as well as the blanket of vegetation over the region, which allows for increased evapotranspiration as moisture is cycled from the vegetation into the atmosphere through surface fluxes. Many studies have analyzed the effects of tropical convection (and associated latent heat release) on the large-scale atmospheric circulation (e.g. Matsuno, 1966; Gill, 1980; Hartmann et al., 1984; Mapes, 1993; Shige and Satomura, 2000; Schumacher et al., 2004), ultimately showing that precipitation events play a critical role in large-scale atmospheric dynamics; thus, it can be assumed that associated latent heat release into the atmosphere in the Amazon fuels the rising branches of the meridional Hadley circulation (which is composed of rising motion in the tropics and sinking motion in the subtropics) and the zonal Walker circulation over the Atlantic.

The Walker circulation is defined as a pattern of steady vertical overturning, initiated by convection occurring over tropical land and descending over the adjacent ocean basin (e.g. Geisler, 1981). It is purported to be sensitive to the latent heating distribution in the vertical, since the atmospheric dynamical response is highly sensitive to the vertical structure of latent heating (Hartmann et al., 1984; Schumacher et al., 2004). Thus, it is not necessarily the surface rain amount but instead the vertical distribution of heating associated with the rain event that has a stronger effect on the atmosphere (Haynes and McIntyre, 1987). While the main Walker cell occurs over the Pacific Ocean, a weaker Walker cell occurs over the Atlantic.

The Atlantic Walker circulation rises over equatorial South America and continues in westerly flow aloft, with sinking motion over the eastern Atlantic Ocean and return flow in the form of surface easterlies. As such, the tropical Atlantic is largely dominated by the trade winds, or winds that blow steadily towards the equator from the northeast in the northern hemisphere, and from the southeast in the southern hemisphere (zonally out of the east), converging in a belt of low pressure called the intertropical convergence zone (ITCZ).

1.2 Connection of convection to environmental variables

For decades, the scientific community has struggled with the unifying question of how air-sea interactions in the tropics affect processes on either side of the atmospheric-oceanic interface, with model representations of the coupling of the two continually being calibrated and developed. A primary area of study that remains unresolved involves how convective processes are related to surface-level winds, sea level pressure (SLP), and sea surface temperatures (SSTs). Understanding these relationships is vital for forecasting tropical rainfall and regional weather patterns (including tropical cyclone development and evolution) due to the correlation between surface convergence, SST, and precipitation.

Two paradigms have emerged as a result - the Lindzen-Nigam approach and the Gill approach - with both attempting to elucidate the tropical atmosphere's response to radiative heating. Under the Lindzen-Nigam approach (Lindzen and Nigam, 1987; Battisti et al., 1999; Back and Bretherton, 2009), it is assumed that higher SSTs produce sensible heat and evaporative fluxes, which subsequently lead to virtual temperature anomalies near the surface that are rapidly mixed into the boundary layer. Changes in the surface pressure gradient occur as a result, that then lead to changes in low-level circulation patterns. It is assumed that deep convection does not strongly affect surface circulation patterns, but serves only as a venting process for the surface heat. However, it is important to note that

many of these studies focused on testing how well models simulated Pacific conditions, not Atlantic conditions, and for open water areas rather than closer to the coasts or even terrestrial areas affected by continental processes (such as the Amazon).

According to the Gill paradigm (Gill, 1980; Battisti et al., 1999), the circulation within the tropical atmosphere can be explained by a set of linearized equations of motion, damped by radiational cooling and mechanical friction, and forced by deep convection. This approach incorporates the effect of the principal sources of heating in the tropics being over land areas (e.g. Ramage, 1968). Convective heating anomalies are closely linked to SST anomalies, such that anomalies in the surface circulation patterns directly result from changes in deep convection. For the purposes of this study, since the effects of deep convection over South America on the Walker circulation are of main focus, a Gill framework will be assumed.

Most past research has focused on observing and modeling the surface-level winds, SSTs, and SLP in the equatorial Pacific due to its much larger size relative to the Atlantic, as well as the interannual variations introduced by the El Niño-Southern Oscillation (ENSO), which impacts weather patterns worldwide through teleconnections. In more recent years, focus has been placed on the Atlantic basin in an effort to determine how differing model approaches should be tailored and modified to accurately reproduce surface-level winds, SSTs, and SLP. This region is of key importance due to the propensity for environmental variables to determine how conducive a region is to tropical cyclone development and intensification. Fortunately, the equatorial Atlantic can be compared to the equatorial Pacific in many regards. For example, both have a cold tongue in the east featuring a shallow thermocline (and thus shallow mixed layer) that is susceptible to changes in upwelling/downwelling and large temperature fluctuations and a warm pool in the west that has a much deeper thermocline and is more stable with respect to surface temperature change. These thermal patterns are a result of dominant surface easterlies across each

basin, unlike the Indian Ocean, which often experiences surface westerlies.

An empirical orthogonal function (EOF) is a statistical decomposition of a dataset or signal into orthogonal basis functions. A major benefit of EOF analysis is that it can reveal patterns in time and space that contribute significantly to the overall variability in a region. With respect to the tropical Atlantic, an EOF analysis was conducted by Nobre and Shukla (1996) using SST and wind stress data from 30^{o}N to 30^{o}S within the Comprehensive Ocean-Atmosphere Dataset (COADS) 2^{o} by 2^{o} grid for the period January 1950 through December 1987 and horizontal winds at six levels from the National Meteorological Center (NMC) operational analysis for the period of June 1974 through December 1987. This study revealed that warmer (colder) off-equatorial SSTs are associated with weaker (stronger) trade winds, and variations in the strength of trades are the primary forcing for thermal changes in the upper ocean. Meridional gradients of anomalous SSTs are most intense during March-April-May (MAM), mainly due to the large SST anomalies over the northern tropical Atlantic during this season. Subsequently, there are strong cross-equatorial wind stress anomalies during MAM, as can be seen in Fig. A.1. Additionally, a relationship between the meridional wind stress and SSTs suggest that anomalous SSTs are locally induced by wind-driven upwelling off the West African coast. Another relevant outcome was that meridional winds and convergence are more strongly influenced by SST gradients (similar to Chiang et al. (2001), but zonal winds tend to be more influenced by deep-tropospheric processes (Back and Bretherton, 2009)).

1.3 Model bias in the Atlantic

Models chronically suffer in reproducing conditions across the tropical Atlantic, with notable and persistent biases appearing in simulations of SST (DeWitt, 2005), SLP (Chang et al., 2007; Richter and Xie, 2008), and surface easterlies (DeWitt, 2005). In particular, a majority of the Coupled Model Intercomparison Project phase 3 (CMIP3) and phase 5

(CMIP5) models exhibit a severe bias in reproducing these variables (Richter and Xie, 2008; Richter et al., 2014). Both generations of models suffer from a westerly bias in surface winds in MAM near the equator (Fig. A.2, vectors) and subsequent difficulties in reproducing the eastern equatorial cold tongue in summer months. Richter et al. (2014) examined how various models handle the equatorial Atlantic to determine the amount of progress made between CMIP3 and CMIP5. They found that there has been some progress in decreasing equatorial Atlantic wind and SST biases, and that the heating in the mid-troposphere due to the location of the ITCZ has a strong influence on surface wind patterns, in line with the aforementioned Gill approach. During the seasonal cycle, as well as during interannual variations, equatorial easterlies intensify when the ITCZ moves north from the equator; however, when the ITCZ is south of the equator, the same easterlies are significantly weaker. It is interesting to note that a maximum in wind variability seems to precede a maximum in SST variability, which cannot be fully explained by the SST-wind component of the Bjerknes feedback that would suggest the eastern equatorial Atlantic SSTs affect the western equatorial Atlantic winds, so further analysis remains.

In addition to a westerly wind bias over the tropical Atlantic, these global climate models (GCMs) exhibit a substantial dry bias over the eastern Amazon during its boreal spring wet season (Fig. A.2, shading). Multiple studies have proposed that a dry bias in Amazonian and coastal South American rainfall can lead to models producing weaker trade winds over the equatorial Atlantic (Richter and Xie, 2008; Tozuka et al., 2011; Richter et al., 2012). Incorrect approximations for surface winds can, in turn, impact SSTs and SLP variations over the equatorial Atlantic. These results are significant, considering the impact continental convection can have on equatorial easterlies (Richter et al., 2014).

1.4 Objective

The goal of this study is to determine whether a strong coupling can be observed between seasons of enhanced precipitation and associated latent heat release over the Amazon and variations in zonal winds, SST, and SLP measured over the tropical Atlantic as a consequence of an intensification of the Walker circulation. During periods of enhanced precipitation, more latent heat is released over the Amazon. It is expected that the rising branch of the Walker circulation would thus intensify, increasing the overturning of the circulation as a whole. Greater surface pressures would result over the east Atlantic as more mass subsides in the sinking branch, thus yielding stronger easterly winds and cooler SSTs across the equatorial Atlantic.

2. DATA AND METHODS

2.1 Spatial domains

The Observations and Modeling of the Green Ocean Amazon experiment (GOAmazon2014/5; Martin et al., 2016) was a large international field campaign that took place in the central Amazon from January 2014 to December 2015 to collect observations to better understand the dynamics and effects of aerosol and cloud life cycles over tropical rainforests. Enhanced observations were gathered during two 40-day intensive operation periods (IOPs) in 2014, during the wet (IOP1 - Feb/Mar 2014) and dry (IOP2 - Sep/Oct 2014) seasons. These IOPs allowed for the greatest amount of seasonal variation in precipitation to be analyzed, since rainfall is approximately 300 mm per month in the wet season and closer to 100 mm per month during the dry season (Tanaka et al., 2014). The Sistema de Proteção da Amazônia (SIPAM) S-band Doppler radar, located in Manaus (yellow star in Fig. A.3), provided three-dimensional reflectivity data up to a 110 km radius from the radar. However, since latent heat release over the Amazon occurs over a much larger spatial area than a single ground radar domain would represent, a larger box for analysis of Amazon rain and latent heating using satellite information from the Tropical Rainfall Measuring Mission (TRMM) radar is considered. Since the SIPAM radar is located at 3.15^{o}S, 59.99^{o}W, the Amazon area of interest was selected to be, in accordance with the 2.5^{o} grid resolution of the TRMM satellite data, 1.25^{o}S to 8.75^{o}S and 63.75^{o}W to 53.75^{o}W, and is represented by the red box in Fig. A.3.

An additional area of interest was selected over the northeastern coast of South America where CMIP3 and CMIP5 models severely underestimate rainfall, as discussed in Richter and Xie (2008) and Richter et al. (2014)(Fig. A.2). If models are misrepresenting rainfall rates and accumulations, associated latent heat release to the atmosphere and sub-

sequent vertical motion fueling the rising branch of the Walker circulation are also likely to be misrepresented. Thus, in accordance with Fig. A.2, the Richter and Xie area of interest is selected to extend from 8.75^{o}N to 3.75^{o}S, 58.75^{o}W to 46.25^{o}W, and is represented by the green box in Fig. A.3. Lastly, for analysis of environmental variables over the Atlantic, spatial focus will be on a latitudinal swath extending from 2.5^{o}N to 2.5^{o}S and 40^{o}W to 10^{o}W (Fig. A.3, blue box), where return flow from the Walker cell and thus effects on the near-surface environment are to be expected.

2.2 TRMM satellite and rain type classification

Latent heating processes are not directly measurable by current remote sensing or in situ instrumentation, but information from radar can be used to estimate latent heating profiles associated with precipitating cloud systems. TRMM was a joint U.S. (National Aeronautics and Space Administration (NASA))-Japanese (Japan Aerospace Exploration Agency (JAXA)) Earth probe satellite launched in late 1997 and in orbit through 2014 and served as the first multi-instrument platform to gather long-term information relating to tropical precipitation on a global scale. In particular, JAXA's Ku-band precipitation radar (PR) onboard the TRMM satellite collected high-quality multi-level rain data that has been used to complete TRMM's key goals of i) better understanding relationships between global energy budgets and the water cycle (Kummerow et al. 2000) and ii) resolving the four-dimensional (spatial-temporal) distribution of latent heating throughout the tropics (Simpson et al., 1988, 1996).

The three-dimensional structure of radar echo is beneficial for determining the organization of precipitating cloud clusters (Houze, 1982, 1989), and thus the rain type occurring at a given location. Tropical rain can be separated into two kinematically and micophysically different types, convective and stratiform (Houze, 1997). Convective rain typically occurs in the form of localized cells on the order of one kilometer in width (Byers and Bra-

ham, 1948) and stratiform rain typically occurs as a more horizontally homogeneous structure spanning more than a hundred kilometers and with a bright band signature present (i.e., a layer of higher reflectivity where snow is melting into rain; Battan, 1973). Each rain type has different growth mechanisms - convective rain tends to form from collision-coalescence processes while stratiform rain grows more by vapor diffusion (Houze, 1997) - such that the structure of latent heat released to the atmosphere can be highly variable (Houze, 1989); however, convective and stratiform rain often occur simultaneously in deep convective systems.

Schumacher and Houze (2003b) demonstrated that it is possible to identify convective and stratiform rain patterns across the tropics with high fidelity using TRMM PR observations. These rain types are identified as the modes that account for the majority of the dynamical atmospheric response to heating (Mapes and Houze, 1995). Since each precipitation type has a distinct profile of latent heating, this becomes vital in determining the effects latent heating has on the larger scale atmospheric circulation (Lau and Peng, 1987; Nakazawa, 1988; Sui and Lau, 1989; Emanuel et al., 1994; Yanai et al., 2000; Sumi and Nakazawa, 2002; Schumacher et al., 2004).

2.3 Latent heating calculation - SHK method

The TRMM PR 2A23 algorithm (Awaka et al., 1997) determines the existence of a bright band, which is indicative of stratiform rain. If present, the algorithm then establishes the bright band height and classifies the pixel as stratiform. The 2A23 algorithm then uses a horizontal texture method based on Steiner et al. (1995) to classify the convective pixels, where intensity and peakedness of maxima in horizontal patterns determine the location of convective cores. In addition to convective and stratiform subdivisions, pixels can also be classified as “other", which typically occurs when there is an anvil aloft and weak to no rain near the surface. A further subdivision occurs for pixels whose echo-top height

is considered shallow, or below the melting level height (termed “shallow convective"; Schumacher and Houze, 2003a; Funk et al., 2013).

The TRMM PR 2A25 algorithm (Iguchi et al., 2000) records information related to radar reflectivity, with an attenuation correction and rain rate for each radar beam approximated through the Hitschfeld-Bordan and surface reference methods. TRMM data with reflectivity values below 18 dBZ were considered marginal (TRMM PR Team, 2011), and thus neglected. The higher quality measurements were then used to create daily 2.5^{o} histogram files stored by the various rain types, which were then aggregated to form monthly multidimensional files containing information across latitude, longitude, height, reflectivity, and storm height.

An individual TRMM PR pixel had a nadir footprint of 4.3 km before the 2001 boost and 5 km after the 2001 boost and 250 m vertical resolution. To determine rain rate, a reflectivity-rain rate (Z-R) relation (Eq. 2.1) is used for each rain type,

$$z = aR^b \tag{2.1}$$

where z = reflectivity, R = rain rate, and a and b are constants, $a_{conv} = 151.1$ and $b_{conv} = 1.584$, $a_{strat} = 255.8$ and $b_{strat} = 1.497$, corresponding to convective and stratiform rain types, respectively (Iguchi et al., 2009). With calculated rain rates for the area of interest, it is then possible to algorithmically determine an approximate latent heating profile. The rate of latent heat release per unit area associated with condensation is:

$$\begin{aligned} &L\left(\frac{change\ of\ mass\ per\ unit\ area}{time}\right) = \\ &L\left(\frac{amount\ of\ water\ accumulating\ on\ unit\ area\ [kg\ m^{-2}]}{time\ [s]}\right) \\ &\sim L(precipitation\ rate\ per\ unit\ area) \end{aligned} \tag{2.2}$$

where L = latent heat of condensation $[m^2\ s^{-2}]$ or $[J\ kg^{-1}]$, and the conversion to precipitation rate utilizes the known density of water ($10^3\ kg\ m^{-3}$). If such latent heat is released into and absorbed by a column of air extending from the surface to around 500 mb (most areas of precipitation on the synoptic scale exist below 500 mb; Sanders and Bosart, 1985) and the latent heat release is evenly distributed with pressure, then the rate of diabatic heating per unit mass with respect to energy is

$$\frac{1}{c_p}\frac{dQ}{dt} \sim \left(\frac{rate\ of\ latent\ heat\ release\ per\ unit\ area\ associated\ with\ condensation}{\frac{1}{2}(p_o/g)}\right) \tag{2.3}$$

where p_0 represents the surface pressure and $p_0/2g$ is the mass of an atmospheric column of unit area extending from the surface to 500 mb (Bluestein, 1992).

In constructing a vertical profile of latent heating, pressure is thus partitioned with intervals of 10 mb. Then the effects of the rain event and the associated latent heat release can be redistributed in the vertical in accordance with idealized profiles (deep convective, shallow convective, and stratiform rain types; Fig. A.4), to reflect the high dependence on the vertical structure of latent heat release. Measurements are then weighted by their respective rain type distributions, with each pressure level receiving a normalized fraction (i.e., stratiform rain fraction, deep convective rain fraction, or shallow convective rain fraction), or frequency, of the total rain. The profiles are then combined linearly to produce the final latent heating profile, fully representative of the breakdown of rain type occurrence.

This method, based on Schumacher et al. (2004) (hereafter SHK), was applied to the Amazon area of interest, and a monthly climatological time series was created for the TRMM-active years of 1998-2014 using rain rates gathered from the pixels comprising the chosen spatial domain (the red box in Fig. A.3). Figure A.5 shows a defined peak in latent heat release during the wet season, or February-March-April (FMA), with a maximum of

150 K/month between 6 and 8 km. Moving into boreal summer, the Amazon experiences a substantial decrease in latent heat release in both magnitude and height, with a maximum of 70 K/month between 5 and 6 km during the July-August-September (JAS) period. The transition from the dry to the wet season (October through December) is more gradual than the shift from wet to dry, which has a steep decline around June before a more gradual decrease from July to the minimum in August.

2.4 Latent heating calculation - CSH and SLH methods

While the idealized profiles from the SHK method provide a reasonable estimate of latent heating across the tropics, several other TRMM-based algorithms have been developed to determine latent heating profiles using lookup tables derived from cloud-resolving models (CRMs). CRMs help elucidate how clouds interact with the environment, and as such, incorporate sub-grid scale physical parameterizations for microphysical processes, radiative transfer, surface fluxes, and turbulent transports.

The two TRMM algorithms that are used most often are the convective-stratiform heating (CSH; TRMM product 3H31) algorithm (Tao et al., 1993, 2000, 2001, 2006, 2010) and the spectral latent heating (SLH; TRMM product 3H25) algorithm (Takayabu, 2002; Shige et al., 2004, 2007). The CSH algorithm incorporates information from the PR and TRMM Microwave Imager (TMI); however, the SLH algorithm only uses information gathered from the PR. The CSH algorithm uses surface rain rate and convective and stratiform rain fractions, which differs from the SLH algorithm in that the latter incorporates an anvil (deep stratiform with a melting level) classification in addition to convective and stratiform classifications, precipitation-top heights, and rain rate at the melting level. The anvil inclusion allows for the calculation of heating even in periods of no measured surface precipitation, while the other parameters allow for a more complex lookup table. Monthly data collected for CSH and SLH were each averaged to create a climatology similar to that

of the SHK method shown in Fig. A.5.

As shown in Fig. A.6, the CSH monthly latent heating profiles over the Amazon indicate that CSH also has a peak in latent heat release between 6 and 8 km during the FMA wet season, although the CSH peak magnitude is somewhat larger (220 K/month) than the SHK peak (150 K/month). Like SHK, CSH also has a pronounced decrease in latent heat release through May and June, with a more gradual taper into the dry season following in the months of June through August. After the August minimum, there is a steady increase back to the wet season in FMA. However, it is unclear why CSH indicates a relative minimum around 4 km during February.

To explain the peak magnitude differences between the two latent heating methods, SHK and CSH monthly stratiform rain fractions are displayed in Fig. A.7. Throughout the year, CSH consistently identifies more rain as stratiform than SHK. This difference is due to the SHK input using modified rain types as suggested by Funk et al. (2013). Specifically, Funk et al. (2013) labels all shallow, non-isolated rain as convective since shallow rain can only be associated with warm rain processes in the tropics (Schumacher and Houze, 2003b). The rain inputs are also different because SHK uses rain calculated from fixed Z-R relations, whereas CSH uses rain input directly from the 2A25 product, which uses varying Z-R relations. The CSH rain input is further modified to match the TMI observations. However, approximations for overall precipitation for the two methods are similar (not shown). Stratiform rain is characterized by a peak in latent heat release to the environment around 8 km and cooling below 5 km (Fig. A.4). Thus, with the higher CSH stratiform rain fractions, it would be expected that the 6-8 km layer would experience higher magnitudes of latent heat release.

The SLH V7A files provide a LHmean variable, as well as variables that correspond to the subdivision of column latent heating into the respective contributions from each rain type (i.e., shallow convective, deep convective, and stratiform). Figure A.8 shows

the monthly climatology for the total heating using variable LHmean. As evidenced by the figure, the general structure of the climatology agrees with that of SHK and CSH; however, subtle variations exist. While the pattern of the peak shifting upward into the wet season and downward into the dry season is in stronger agreement with the SHK algorithm, the peak of latent heat release is slightly higher in elevation, centered around 8 km. The magnitudes of latent heat release are also comparable to that approximated by CSH, with around 130 K/month during the wet season and around 60 K/month during the dry season.

The SLH files do not include the input surface rain rate or stratiform rain fractions with which to compare to the SHK and CSH inputs (e.g., Fig. A.7), so Fig. A.9 plots the component profiles for March (top) and August (bottom) for SHK (left) and SLH (right). The total profiles for all the techniques are also included.

For March, it is most evident that while similar in magnitude below 6 km, SLH identifies a more pronounced peak in stratiform heating than SHK above 6 km; the stratiform component of SLH is approximately 30-40 K/month larger than that of SHK. The shallow convective heating profile (dotted) is less than 10 K/month throughout; however, the shallow component of SHK is closer to 10-20 K/month. As a result, SLH has less shallow convective heating close to the surface and more stratiform heating aloft relative to SHK, yielding a higher peak in total column latent heat release. While both SHK and SLH measure similar magnitudes for the deep convective component (solid black) below around 4 km, the SLH features a stronger drop off above the 4-5 km peak and the SHK features a more gradual decrease such that there is consistently stronger deep convective heating above 5 km in the SHK approximation. Though SLH has a greater amount of stratiform heating aloft leading to an overall total heating peak being at a higher elevation, SHK has a greater amount of deep convective heating above 4 km. Therefore, in comparing magnitudes of total heating, the additional stratiform contribution of SLH aloft is offset by

the deep convective contribution in SHK, yielding similar amounts of total column latent heating from around 8 km up. However, SLH is much smaller in magnitude lower in the column relative to SHK due to less deep convective heating.

For August, the SLH has a much higher stratiform component of heating throughout the entire profile; the algorithm estimates more heating aloft and more cooling at the surface than SHK. However, deep convective heating is much larger in the SLH dataset, especially between 3 and 6 km. The shallow convective components of SHK and SLH are very similar. Therefore, SLH measures slightly more total heating above 6 km, but heating comparable to SHK below 6 km due to increased deep convective and stratiform heating that act to offset one another.

Overall, the most influential discrepancies between the total profiles of the two methods can be attributable to the SLH algorithm measuring a greater stratiform warming aloft and having a more sudden decrease in deep convective moving upward and away from the level of peak deep convective heating. It is clear that the total heating profile for CSH is much larger in magnitude than both SLH and SHK, likely due to variations in the lookup tables used to construct the algorithm.

2.5 GoAmazon2014/5 field campaign

Where available, it is beneficial to analyze continuous, in situ measurements, which can aid in validating the accuracy of precipitation and latent heating estimates derived from satellite, as well as provide more detailed storm structure at finer time and space scales. During GOAmazon2014/5, the SIPAM Doppler radar located in Manaus (the star in Fig. A.3) provided consistent three-dimensional reflectivity measurements throughout the campaign. Using this radar data, rain rates were determined using a reflectivity-rainrate (Z-R) relation derived from disdrometer observations made near the SIPAM site.

The SHK algorithm was applied to SIPAM surface rain rates, which were separated

into convective and stratiform rain types using the method of Fliegel (2012) and averaged for each month of 2014 within a 110 km radius of the radar. A 15-km mask was applied to the inner circle closest to the location of the radar to eliminate the cone of silence and interference from trees and buildings. Additionally, data within the date range of November 2-11, 2014 was discarded due to technical difficulties with the radar and false reflectivity measurements. Finally, the SIPAM rain type separation does not include a shallow convective classification because the lack of upper level sweeps in many of the volume scans precluded the ability to calculate heights for all raining pixels.

The SIPAM monthly averaged latent heating time series for 2014 is shown in Fig. A.10. The strongest peak is observed across the FMA wet season between 6 and 8 km and reaches 230 K/month. There is an abrupt decrease between May and June followed by a more gradual decrease into the minimum, which occurs around August and September. This evolution is similar to the long-term climatologies derived from the SHK, CSH, and SLH methods applied to the TRMM PR data (Figs. A.5, A.6, and A.8 respectively) over a larger spatial domain (Fig. A.3). However, there is a more pronounced minimum just above the surface (between 0 and 2.5 km) in the SIPAM data set during the wet season. The SIPAM data only covers one year so it could experience more extreme values of stratiform rain fraction compared to the 16-year TRMM climatology, which would lead to enhanced cooling at low levels. In addition, since the SIPAM rain type classification does not subdivide the convective pixels into deep and shallow, latent heat release in the low levels due to shallow convective rain is not taken into account. There is also an October maximum in the transition season that is not seen in the other datasets, but this only represents data for 2014 so deviations away from the climatological pattern are to be expected. Overall, the ground radar latent heating estimates seem to be in agreement with the SHK, CSH, and SLH TRMM climatologies.

2.6 Variational analysis

Heating can additionally be quantified through a variational analysis approach (Zhang and Lin, 1997; Zhang et al., 2001), where minimal adjustments are made to a small network of sounding measurements - in particular, winds, temperature, and water vapor mixing ratio - to force the atmospheric state variables to satisfy mass, moisture, energy, and momentum balances. Surface rain and top-of-atmosphere radiation observations are major constraints to the variational analysis model. The goal of multiple studies using a variational analysis method (e.g. Schumacher et al., 2007; Xie et al., 2010) is to study the sensitivity of diagnostic variables such as apparent heat sources (Q_1) and moisture sinks (Q_2) to determine how the environment is warmed and dried by convective processes (Yanai et al., 1973). Q_1 represents the interaction between radiative heating, eddy sensible heat transport, and latent heat release from cloud and precipitation systems. Since the latent heat release component is an order of magnitude larger than the other two (Houze, 1982), Q_1 can be compared to latent heating retrievals such as from the SHK, CSH, and SLH methods.

For GOAmazon2014/5, the variational analysis domain was a 110-km radius centered on the SIPAM radar. Precipitation data from the radar was gathered with a 3-hour temporal resolution during the two IOPs, then combined with European Center for Medium range Weather Forecasting (ECMWF) analyses as background and surface/top of atmosphere constraints (due to the lack of a network of sounding measurements), with the goal of understanding seasonal variability of large-scale heat and moisture budgets associated with Amazonian convection.

As a way of verifying the satellite and ground radar latent heating methodologies, the TRMM-based CSH and SLH datasets, the SIPAM radar dataset using the SHK method, and the variational analysis were analyzed for each of the IOPs for the Amazon area of

interest. For the variational analysis dataset, a rain rate threshold of all events greater than 0.2 mm/hr was applied so that only measurements denoting a period of precipitation were incorporated into the average across each IOP. This threshold was especially applied to limit contamination of the SIPAM rain rates by ground clutter. For comparison purposes, each heating retrieval was plotted individually to observe variations between the two IOPs (Fig. A.11), and the four algorithms are then plotted for each IOP to determine how well they agree (Fig. A.12).

Figure A.11 shows that the latent heat release is greater during IOP1 (solid lines) than during IOP2 (dashed lines) because IOP1 occurred during the wet season. The height of peak latent heat release is higher during IOP1 than IOP2 for all algorithms because of the higher stratiform rain contributions in IOP1. There is also more low-level heating in all of the retrievals during IOP1 from enhanced shallow convection except for SIPAM due to the fact that the SIPAM retrieval does not have a shallow classification because of deficiencies in the echo-top classification for some of the radar volumes.

Figure A.12 shows that the general shape of the heating retrievals are in good agreement during both IOPs; however, the magnitudes are higher for the variational analysis throughout all levels potentially due to the inclusion of the other diabatic heating components, but more likely because of the 0.2 mm/hr threshold that was applied to remove hours with light rain rates retrieved from excessive ground clutter over the radar domain. The magnitudes of the SLH profiles for both IOP1 and IOP2 are significantly less than that of the other three, possibly due to higher contribution of stratiform heating. Overall, the four datasets are in general agreement for this region of Amazonia, with most variation attributable to differences in rain type identification and rain inputs.

3. AMAZON HEATING AND THE ATLANTIC GENERAL CIRCULATION

3.1 Heating over Richter and Xie area of interest

To focus on potential effects from model underestimation of latent heat release to the atmosphere, the Richter and Xie area of interest (Fig. A.3, green box) was chosen as the spatial domain to represent the rising branch of the Walker circulation. The SHK method (which was shown to be a valid heating retrieval over the central Amazon in the previous chapter) was applied to the TRMM PR climatology in this region, and a contoured plot for monthly latent heating is shown in Fig. A.13. Here, the peak in latent heating is still in the 6-8 km range, but now the season of greatest latent heat release is shifted a month later and a month longer to March-April-May-June (hereafter MAMJ). The magnitude of greatest latent heat release, observed during each of the locations' respective wet seasons, is slightly lower over the Richter and Xie domain, likely due to the impact of vegetation within the Amazon area of interest increasing rain amounts over the Amazon and the lower amounts of stratiform rain over the Richter and Xie domain that shift the heating more equally in the vertical (Fig. A.14).

Since the elevation of peak latent heat release occurs around 7 km, and the rainy season occurs during MAMJ (Fig. A.13), latent heating at 7 km was averaged across MAMJ for each year, and years were subsequently ranked by magnitude of average latent heat release. Years were then identified as having experienced relatively high or low latent heating averages as compared to the other years and the dataset was split in half as follows, with the median year being classified based on whether or not it was numerically closer to the next highest value or the next lowest value (Table B.1).

Latent heating data calculated using the SHK method was averaged for the newly partitioned subsets (high and low) to produce two climatological plots of latent heating profiles

(Fig. A.15). During the high years, months with strong heating extend from February to June with a peak heating of 130 K/month in May. During the low years, latent heating peaks in April and May with a maximum magnitude of 90 K/month; there is also a secondary peak in February of 80 K/month. Both high and low years decrease to a minimum of 40 K/month by September, with the wet years starting the transition season a month earlier than the dry years (October versus November). This earlier ramp up may be due to the enhanced rainfall earlier in the year that would impact land surface conditions and land-atmosphere interactions through the dry season.

3.2 Atlantic climatology from reanalysis

In situ observations are generally considered being most representative of reality; however, collecting meteorological data over the open ocean can be difficult, with surface measurements only available along ship tracks and from a sparse network of buoys and islands. Upper air observations are even more sparse. To obtain more spatially and temporally consistent data over the tropical oceans, reanalyses are generally used. Reanalyses assimilate observations but are inherently model based, and can thus be subject to error introduced by parameterizations of smaller scale processes. However, they are the best option to represent the climatology of the large-scale atmosphere for regions such as the tropical Atlantic. In particular, data from the Modern-Era Retrospective analysis for Research and Applications version 2 (MERRA-2) is used in this study.

To better understand background changes in the meteorological variables of interest across the Atlantic basin, climatological averages were calculated for April and June. April represents a time during the peak Amazonian wet season when one would expect to see increased vertical motion in the west (Figures A.16 and A.17, left column). June features the summer solstice, when seasonal peak incoming radiation and the location of the ITCZ is furthest north; this represents a relative extreme when the equatorial region is

less affected by the zonal trough (Figures A.16 and A.17, right column).

Between April and June, there is a northward shift of peak SSTs from being located between 5^{o}S and the equator to between the equator and 5^{o}N (Fig. A.16, top row). Whereas there are higher SSTs off the west coast of Africa in April, representing the highest values of the basin, the emergence of the equatorial cold tongue appears in June as the ITCZ moves northward from the area, featuring the lowest values of the basin.

In looking at SLP (Fig. A.16, bottom row), there are pronounced peaks across the north and south Atlantic gyres, on either side of the equatorial trough. In June, SLP almost uniformly intensifies throughout the entire Atlantic basin and features a slight shift to the north, especially in the east, in agreement with the northward shift in the ITCZ. It remains unclear why basin-wide values are significantly higher in June relative to April.

The presence of strong trades through the tropics can be seen in the top row of Figure A.17, with cool colors extending from 30^{o}S to 30^{o}N, which signify negative values and thus a westward flow of air. Outside of the tropics, a transition to prevailing westerlies can be seen with the presence of warmer colors. In June, the regions of peak easterly winds are much stronger than in April, with stronger easterlies in the west as air flows into the region of convergence in northern South America, which intensifies and fuels the rising branch of the Walker cell. Coincident with the seasonal migration of the ITCZ, the doldrums are near-equatorial in April, then shift north to a location around 5^{o}N in June.

In looking at 500 mb omega (Figure A.17, bottom row), the equatorial trough is the most prominent feature with the largest magnitudes of upward motion (shown by the cooler colors; negative omega implies positive vertical motion), indicating the location of the ITCZ. In April, the ITCZ is approximately equatorial, and then shifts northward to approximately $5 - 10^{o}$N in June. There is stronger vertical motion in the west (over northern South America) in April, and much less over the same region in June. The north and south Atlantic gyres experience a nearly uniform subsidence of air, which is in agreement

and is collocated with the areas of high SLP.

3.3 Atlantic circulation variability based on high and low heating years over the Amazon

For the subsets of high and low years (Table B.1), zonal wind, SLP, and SST data from MERRA-2 is averaged for an elongated swath along the equator and extending directly across the Atlantic Ocean, from 40^{o}W to 10^{o}W, 2.5^{o}N to 2.5^{o}S, or the region of the tropical Atlantic where the return flow of the Walker cell is to be expected (Fig. A.3, blue box). Additionally, 500 mb omega is plotted to verify relative magnitudes of rising motion. For each of the variables of interest, data was averaged across latitudes within the spatial domain, such that longitudinal variations would be highlighted.

3.3.1 Omega

Figure A.18 shows the annual cycle of omega at 500 mb for the high (top) and low (middle) heating years, as well as the difference in omega between the high and low heating years (bottom). During both the high and low years, there is significant rising motion (represented by negative values) in the western Atlantic and weaker rising motion in the eastern Atlantic during the wet season months of January through May, with maximum rising motion during the month of April (the time of maximum heating over the Amazon). Positive vertical motion is still seen in the east during this period due to the presence of warm waters and troughing along the equator during these months (represented by April plots in Figures A.16 and A.17), but it is much smaller in magnitude relative to the west. Sinking motion (positive values) occurs across the equatorial Atlantic during the Amazonian dry season (July through November) as warm waters and the equatorial trough move northward (represented by June plots in Figures A.16 and A.17). During MAM, Horel (1982) showed that the ITCZ is approximately over the equator, but by August and September, the ITCZ is further north, around 12^{o}N; thus, rising motion is significantly

diminished.

During high heating years (Fig. A.18, top panel), the easternmost area transitions to sinking motion in June while the westernmost area sees sinking motion in mid- to late July. This lag can be explained by the magnitudes of rising motion - since the westernmost areas experience stronger rising motion, the switch to positive values for omega takes longer. For the low heating years (Fig. A.18, middle panel), the pattern is largely the same, except the magnitudes are significantly lower during MAM, leading to an earlier switch to sinking motion as the dry season approaches (occurring in early July).

The difference plot (Fig. A.18, bottom panel) illuminates the largest changes in 500-mb omega that are associated with high and low heating years in the Amazon; in particular, cooler colors during MAM signify the high years having stronger upward motion, and warmer colors signify the low years having stronger upward motion. Upward motion is stronger in the west (between 40^{o}W and 35^{o}W) during most months for years of high latent heat release (even though high and low years were classified based on heat release during the wet season). This stronger latent heat release in the west appears to correlate with stronger sinking in the eastern equatorial Atlantic throughout the year. This is consistent with years of high latent heat release experiencing an enhancement of the Walker circulation, which correlates with greater rising motion in the west and greater subsidence in the east. However, during low heating years, February shows stronger upward motion in the western Atlantic and stronger downward motion in the central Atlantic and April shows stronger downward motion across the central and eastern Atlantic. These vertical motion anomalies are likely due to the evolution of heating during the low heating years, which has an early maximum in heating during February and an early pick up in the main maximum in April (Fig. A.15).

3.3.2 SLP

For both high and low heating years, there is a significant lag between the increased latent heat release during MAMJ in the Richter and Xie area of interest and the increase in SLP detected for the eastern tropical Atlantic (Fig. A.19, top and middle panels). While SLP is fairly constant across the MAMJ wet season, with even slightly lower pressures in the east, the biggest change occurs toward the end of the wet season, between April and June, when SLP across the tropical Atlantic nearly uniformly experiences an increase, which also coincides with the seasonal departure of the ITCZ from the equatorial Atlantic. Associated rising motion and thus lower surface pressures have migrated northward at this point, and as a result, relatively higher pressures result at the surface. The largest longitudinal variation occurs from July to August, with the highest values in the east and lower values in the west.

The SLP difference plot (Fig. A.19, bottom panel) shows significant zonal striation during the wet season, representing a switch between the high years experiencing stronger SLP readings and the low years experiencing stronger readings. The months when SLP is higher are when there are latent heating local maxima during the low years (i.e., February and June). During the dry season, there are no significant oscillations. It is interesting to note that from June to September, SLP is higher for the years when latent heat release from the Richter and Xie area of interest was lower. Thus, there may be implications for boreal spring Amazon heating on hurricane formation conditions during boreal summer.

3.3.3 Zonal wind

The annual cycle of zonal wind speed for both high and low heating years show similar variations in equatorial easterlies across the Atlantic (Fig. A.20, top and middle panels). During a period when pressure is zonally constant (e.g. from April to June) there is little longitudinal variation in the magnitude of zonal winds, which is consistent with the magni-

tude of the pressure gradient (Fig. A.19). Winds are weaker in April due to the dominance of the ITCZ and associated weak horizontal winds. As the ITCZ departs and pressure increases to its peak in June through September, zonal winds become stronger as the Walker cell assumes dominance. The stronger pressure gradient in the west corresponds to a convergence of air into an area of low pressure in northern South America, which leads to the enhanced vertical lift (Fig. A.17) and precipitation totals seen in the region. Conversely, a weak pressure gradient in the east results in weak winds. An additional period when winds are significantly weaker in the east appears during the month of September, likely due to the seasonal migration of peak solar radiation over the equatorial region.

When comparing the high and low years (Fig. A.20, bottom panel), warmer colors represent areas when the low years experience stronger easterlies; cooler colors represent areas when the high years experience stronger easterlies. Overall, the west is dominated by stronger easterlies during low years, and the east is dominated by stronger easterlies during high years. There is a slight oscillation from east to west in peak difference, particularly from January through August and strongest during MAMJ, which can likely be linked to variations in the timing of pressure changes and the subsequent changes in zonal winds.

3.3.4 SST

When analyzing SSTs (Fig. A.21), a structure similar to that of SLP is seen for both high years and low years (top and middle panels), with warm SSTs across the equatorial Atlantic January through May shifting to much cooler waters in the eastern Atlantic from June to October. When the pressure gradient and thus zonal winds are strongest, the SSTs trend lower. The stronger trades, seen from May through August, advect warmer surface water westward, decreasing the depth of the thermocline and allowing cooler subsurface water to upwell.

SST variations between high and low years (Fig. A.21, bottom panel) show that the

west Atlantic is generally warmer and the east Atlantic is generally cooler during high years, consistent with the zonal wind differences in the previous section. The main exception occurs in June when the entire equatorial Atlantic is warmer during high heating years. This signal potentially represents a delay or weakening in the setup of the equatorial cold tongue in the eastern Atlantic in June, linked to changes in the western Atlantic in April and May (e.g. see eastward propagating feature between 40^{o}W and 30^{o}W).

4. CONCLUSIONS

When looking at Amazonia, there is generally good agreement between latent heating retrievals derived from the SHK, CSH, SLH, and variational analysis algorithms, showing a strong wet season during FMA, a dry season during JAS, and peak latent heat release between 6-8 km; however, variations exist due to differences in rain type identification and different sources of rain rates.

Latent heating from the SHK algorithm was analyzed across the Richter and Xie spatial area in the northeastern Amazon, where many GCMs experience severe precipitation biases, and years were classified as having relatively high or low latent heating across the MAMJ wet season. In correlation with higher magnitudes of latent heat release, 500-mb omega values nearest to this area of interest are more strongly negative during boreal spring than during years of lower latent heat release, indicating stronger positive vertical motion and verifying the strongest location of rising motion with a concurrent decrease in upward motion in the eastern Atlantic, as would be expected from a strengthened Walker circulation. A corresponding increase in SLP, an increase in return surface easterlies, and a decrease in SST across the equatorial Atlantic in also observed during boreal spring for high latent heating years.

During the low years, the evolution of heating through the wet season affects the timing and magnitudes of vertical motion, such that an early peak in latent heat release during February and an earlier pick up in the main peak during the month of April yield short but significant enhancements in the Walker circulation. As a result, SLP readings are lower in comparison to the high years during these periods.

When comparing low and high heating years and their impact on the Atlantic Walker circulation, there is significant temporal lag such that the strongest SLP and easterly

anomalies appear in boreal summer during high years. This lag is likely due to the dominance of the equatorial trough over the Atlantic during the Amazonian wet season, which moves north during boreal summer. In addition, high latent heating years show a delay in the onset of the cold tongue in June and July. This feature, in conjunction with the lower SLP, may have an impact on conditions in the equatorial Atlantic during the North Atlantic hurricane season during high heating years over the Amazon.

REFERENCES

Awaka, J., T. Iguchi, H. Kumagai, and K. Okamoto, 1997: Rain type classification algorithm for TRMM precipitation radar. *Proc. 1997 Int. Geoscience and Remote Sensing Symp.*, Singapore, Institute of Electrical and Electronics Engineers, 1633–1635.

Back, L., and C. Bretherton, 2009: On the relationship between SST gradients, boundary layer winds, and convergence over the tropical oceans. *J. Climate*, **22**, 4182–4196.

Battan, L., 1973: *Radar Observation of the Atmosphere*. University of Chicago Press, 324 pp.

Battisti, D., E. Sarachik, and A. Hirst, 1999: A consistent model for the large-scale steady surface atmospheric circulation in the tropics. *J. Climate*, **12**, 2956–2964.

Bluestein, H., 1992: *Principles of Kinematics and Dynamics. Vol. I, Synoptic - Dynamic Meteorology in Midlatitudes*. Oxford University Press, 431 pp.

Byers, H. R., and R. Braham, Jr., 1948: Thunderstorm structure and circulation. *J. Meteor.*, **5**, 71–86, doi:10.1175/1520-0469(1948)005<0071:TSAC>2.0.CO;2.

Chang, C.-Y., J. Carton, S. Grodsky, and S. Nigam, 2007: Seasonal climate of the tropical Atlantic sector in the NCAR community climate system model 3: error structure and probable causes of errors. *J. Climate*, **20**, 1053–1070.

Chiang, J., S. Zebiak, and M. Cane, 2001: Relative roles of elevated heating and surface temperature gradients in driving anomalous surface winds over tropical oceans. *J. Atmos. Sci.*, **58**, 1371–1394.

DeWitt, D., 2005: Diagnosis of the tropical Atlantic near-equatorial SST bias in a directly coupled atmosphere - ocean general circulation model. *Geophys. Res. Lett. 32, L01703*, doi:10.1029/2004GL021707.

Emanuel, K. A., J. D. Neelin, and C. S. Bretherton, 1994: On large-scale circulations in

convecting atmospheres. *Quart. J. Roy. Meteor. Soc.*, **120**, 1111–1143, doi:10.1002/qj.49712051902.

Fliegel, J., 2012: Quality control and census of SMART-R observations from the DYNAMO/CINDY2011 field campaign. M.S. thesis, Texas A&M University, College Station, 84 pp.

Funk, A., C. Schumacher, and J. Awaka, 2013: Analysis of rain classifications over the tropics by version 7 of the TRMM PR 2A23 algorithm. *J. Meteor. Soc. Japan*, **91**, 257–272.

Geisler, J., 1981: A linear model of the walker cell. *J. Atmos. Sci.*, **38**, 1390–1400.

Gill, A. E., 1980: Some simple solutions for heat-induced tropical circulation. *Quart. J. Roy. Meteor. Soc.*, **106**, 447–462.

Hartmann, D. L., H. H. Hendon, and R. A. Houze, Jr., 1984: Some implications of the mesoscale circulations in tropical cloud clusters for large-scale dynamics and climate. *J. Atmos. Sci.*, **41**, 113–121.

Haynes, P. H., and M. E. McIntyre, 1987: On the evolution of vorticity and potential vorticity in the presence of diabatic heating and frictional or other forces. *J. Atmos. Sci.*, **44**, 828–841.

Horel, J., 1982: The annual cycle in the tropical Pacific atmosphere and ocean. *Mon. Wea. Rev.*, **110**, 1863–1878.

Houze, R. A., Jr., 1982: Cloud clusters and large-scale vertical motions in the tropics. *J. Meteor. Soc. Japan*, **60**, 396–410.

Houze, R. A., Jr., 1989: Observed structure of mesoscale convective systems and implications for large-scale heating. *Quart. J. Roy. Meteor. Soc.*, **115**, 425–461.

Houze, R. A., Jr., 1997: Stratiform precipitation in regions of convection: A meteorological paradox? *Bull. Amer. Meteor. Soc.*, **78**, 2179–2196.

Iguchi, T., T. Kozu, J. Kwiatkowki, R. Meneghini, J. Awaka, and K. Okamoto, 2009: Un-

certainties in the rain profiling algorithm for the TRMM precipitation radar. *J. Meteor. Soc. Japan*, **87A**, 1–30.

Iguchi, T., T. Kozu, R. Meneghini, J. Awaka, and K. Okamoto, 2000: Rain-profiling algorithm for the TRMM precipitation radar. *J. Appl. Meteor.*, **39**, 2038–2052.

Kummerow, C., and Coauthors, 2000: The status of the tropical rainfall measuring mission (TRMM) after two years in orbit. *J. Appl. Meteor.*, **39 (12)**, 1965–1982, doi:10.1175/1520-0450(2001)040<1965:TSOTTR>2.0.CO;2.

Lau, K.-M., and L. Peng, 1987: Origin of low-frequency (intraseasonal) oscillations in the tropical atmosphere. Part I: Basic theory. *J. Atmos. Sci.*, **44**, 950–972.

Lindzen, R., and S. Nigam, 1987: On the role of sea surface temperature gradients in forcing low-level winds and convergence in the tropics. *J. Atmos. Sci.*, **44**, 2418–2436.

Mapes, B., 1993: Gregarious tropical convection. *J. Atmos. Sci.*, **50**, 2026–2037.

Mapes, B., and R. A. Houze, Jr., 1995: Diabatic divergence profiles in western Pacific mesoscale convective systems. *J. Atmos. Sci.*, **52**, 1807–1828.

Martin, S. T., and Coauthors, 2016: Introduction: Observations and modeling of the Green Ocean Amazon (GoAmazon2014/5). *Atmos. Chem. Phys.*, **16 (8)**, 4785–4797, doi:10.5194/acp-16-4785-2016.

Matsuno, T., 1966: Quasi-geostrophic motions in the equatorial area. *J. Meteor. Soc. Japan*, **44**, 25–43.

Nakazawa, T., 1988: Tropical superclusters within intraseasonal variations over the western Pacific. *J. Meteor. Soc. Japan*, **66**, 823–839.

Nobre, P., and J. Shukla, 1996: Variations of sea surface temperature, wind stress, and rainfall over the tropical Atlantic and South America. *J. Climate*, **9**, 2464–2479.

Ramage, C., 1968: Role of a tropical “maritime continent" in the atmospheric circulation. *Mon. Wea. Rev.*, **99**, 365–370.

Richter, I., and S.-P. Xie, 2008: On the origin of equatorial Atlantic biases in coupled

general circulation models. *Clim. Dynam.*, **31**, 587–598.

Richter, I., S.-P. Xie, S. Behera, T. Doi, and Y. Masumoto, 2014: Equatorial Atlantic variability and its relation to mean state biases in CMIP5. *Clim. Dynam.*, **42**, 171–188.

Richter, I., S.-P. Xie, A. Wittenberg, and Y. Masumoto, 2012: Tropical Atlantic biases and their relation to surface wind stress and terrestrial precipitation. *Clim. Dynam.*, **38**, 985–1001.

Riehl, H., and J. Malkus, 1957: On the heat balance and maintenance of circulation in the Trades. *Quart. J. Roy. Meteor. Soc.*, **83**, 21–29.

Sanders, F., and L. Bosart, 1985: Mesoscale structure in the megalopolitan snowstorm, 11-12 February 1983. Part II: Doppler radar study of the New England snowband. *J. Atmos. Sci.*, **42**, 1398–1407.

Schumacher, C., and R. A. Houze, Jr., 2003a: Stratiform rain in the tropics as seen by the TRMM precipitation radar. *J. Climate*, **16**, 1739–1756.

Schumacher, C., and R. A. Houze, Jr., 2003b: The TRMM precipitation radar's view of shallow, isolated rain. *J. Appl. Meteor.*, **42**, 1519–1524.

Schumacher, C., R. A. Houze, Jr., and I. Kraucunas, 2004: The tropical dynamical response to latent heating estimates derived from the TRMM precipitation radar. *J. Atmos. Sci.*, **61**, 1341–1358.

Schumacher, C., M. Zhang, and P. Ciesielski, 2007: Heating structures of the TRMM field campaigns. *J. Atmos. Sci.*, **64**, 2593–2610.

Shige, S., and T. Satomura, 2000: The gravity wave response in the troposphere around deep convection. *J. Meteor. Soc. Japan*, **78**, 789–801.

Shige, S., Y. N. Takayabu, W.-K. Tao, and D. E. Johnson, 2004: Spectral retrieval of latent heating profiles from TRMM PR data. Part I: Development of a model-based algorithm. *J. Appl. Meteor.*, **43**, 1095–1113.

Shige, S., Y. N. Takayabu, W.-K. Tao, and C.-L. Shie, 2007: Spectral retrieval of latent

heating profiles from TRMM PR data Part II: Algorithm improvement and heating estimates over tropical ocean region. *J. Appl. Meteor.*, **46**, 1098–1124.

Simpson, J., 1992: Global circulation and tropical cloud activity. *The Global Role of Tropical Rainfall*, J. S. Theon and T. Matsuno, Eds., Hampton, VA (United States); DEEPAK Publishing, 77–92.

Simpson, J., R. F. Adler, and G. R. North, 1988: Proposed tropical rainfall measuring mission (TRMM) satellite. *Bull. Amer. Meteor. Soc.*, **69**, 278–295.

Simpson, J., C. Kummerow, W.-K. Tao, and R. F. Adler, 1996: On the tropical rainfall measuring mission (TRMM). *Meteor. Atmos. Phys.*, **60**, 19–36.

Steiner, M., R. Houze, Jr., and S. E. Yuter, 1995: Climatological characterization of three-dimensional storm structure from radar and rain gauge data. *J. Appl. Meteor.*, **34**, 1978–2007.

Sui, C.-H., and K.-M. Lau, 1989: Origin of low-frequency (intraseasonal) oscillations in the tropical atmosphere. Part II: Structure and propagation of mobile wave-CISK modes and their modification by lower boundary forcings. *J. Atmos. Sci.*, **46**, 37–56.

Sumi, A., and T. Nakazawa, 2002: Satellite monitoring for the season-to-interannual climate fluctuations. *Korean J. Atmos. Sci.*, **5S**, 13–28.

Takayabu, Y. N., 2002: Spectral representation of rain features and diurnal variations observed with TRMM PR over the equatorial area. *Geophys. Res. Lett.*, **29**, 1584.

Tanaka, L. M. d. S., P. Satyamurty, and L. A. T. Machado, 2014: Diurnal variation of precipitation in central Amazon Basin. *Int. J. Climatol.*, **34**, 3574–3584.

Tao, W.-K., S. Lang, J. Simpson, and R. Adler, 1993: Retrieval algorithms for estimating the vertical profiles of latent heat release and their applications for TRMM. *J. Meteor. Soc. Japan*, **71**, 685–700.

Tao, W.-K., S. Lang, J. Simpson, W. Olson, D. Johnson, B. Ferrier, C. Kummerow, and R. Adler, 2000: Vertical profiles of latent heat release and their retrieval for TOGA

COARE convective systems using a cloud resolving model, SSM/I, and ship-borne radar data. *J. Meteor. Soc. Japan*, **78**, 333–355.

Tao, W.-K., S. Lang, X. Zeng, S. Shige, and Y. Takayabu, 2010: Relating convective and stratiform rain to latent heating. *J. Clim.*, **23**, 1874–1893.

Tao, W.-K., and Coauthors, 2001: Retrieved vertical profiles of latent heat release using TRMM rainfall products for february 1998. *J. Appl. Meteor.*, **40 (6)**, 957–982.

Tao, W.-K., and Coauthors, 2006: Retrieval of latent heating from TRMM measurements. *Bull. Amer. Meteor. Soc.*, **87 (11)**, 1555–1572.

Tozuka, T., T. Doi, T. Miyasaka, N. Keenlyside, and T. Yamagata, 2011: Key factors in simulating the equatorial Atlantic zonal sea surface temperature gradient in a coupled general circulation model. *J. Geophys. Res.*, **116(C06010)**.

TRMM PR Team, 2011: *Tropical Rainfall Measuring Mission (TRMM) precipitation radar algorithm Instruction Manual for Version 7*, JAXA–NASA, 170 pp. [Available online at http://www.eorc.jaxa.jp/TRMM/documents/PR_algorithm_product_information/pr_manual/PR_Instruction_Manual_V7_L1.pdf.].

Xie, S.-P., C. Deser, G. A. Vecchi, J. Ma, H. Teng, and A. T. Wittenberg, 2010: Global warming pattern formation: Sea surface temperature and rainfall. *J. Clim.*, **23**, 966–986.

Yanai, M., B. Chen, and W.-W. Tung, 2000: The Madden-Julian oscillation observed during the TOGA COARE IOP: Global view. *J. Atmos. Sci.*, **57**, 2374–2396.

Yanai, M., S. Esbensen, and J.-H. Chu, 1973: Determination of bulk properties of tropical cloud clusters from large-scale heat and moisture budgets. *J. Atmos. Sci.*, **30**, 611–627.

Zhang, M. H., and J. L. Lin, 1997: Constrained variational analysis of sounding data bases on column-integrated budgets of mass, heat, moisture, and momentum: Approach and application to ARM measurements. *J. Atmos. Sci.*, **54**, 1503–1524.

Zhang, M. H., J. L. Lin, R. T. Cederwall, J. J. Yio, and S. C. Xie, 2001: Objective analysis

of ARM IOP data: Method and sensitivity. *Mon. Wea. Rev.*, **129**, 295–311.

APPENDIX A

FIGURES

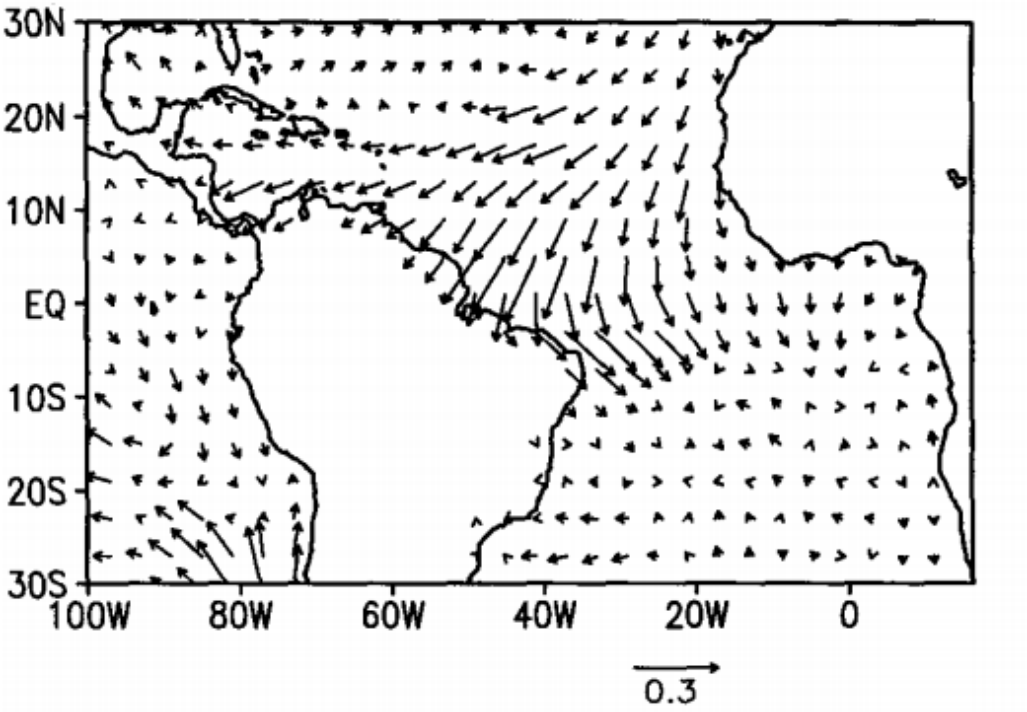

Figure A.1: COLD - WARM composite surface wind stress during MAM; vector in lower right corner represents $0.3\ dyn/cm^2$. Reprinted from Nobre and Shukla (1996).

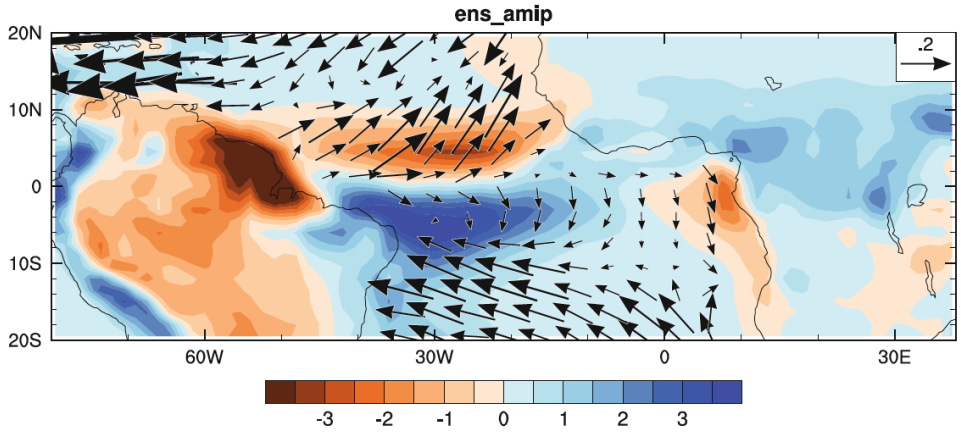

Figure A.2: Climatological MAM biases of precipitation (shading; mm/day) and surface wind stress (vectors; reference vector $0.2\ Nm^{-2} \times 10^{-1}$). Reprinted from Richter et al. (2014).

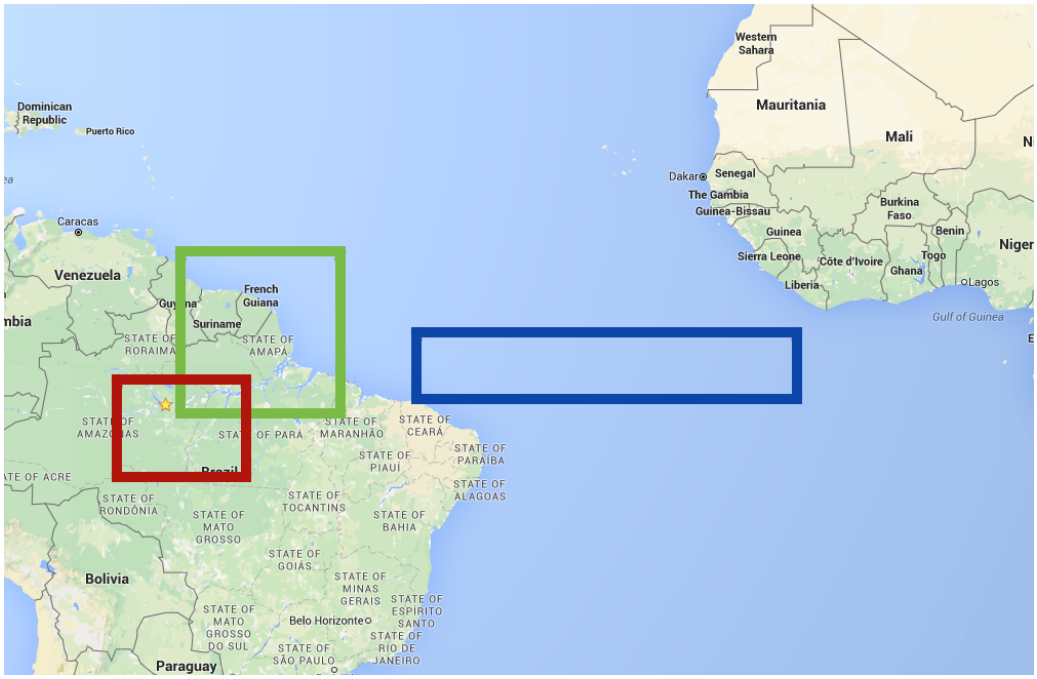

Figure A.3: The location of the SIPAM radar is depicted by the yellow star. An expanded area of interest around the SIPAM radar (in accordance with TRMM-defined pixels) is indicated in **red**, a region of substantial dry bias (defined in Richter and Xie (2008) is shown in **green**, and the region of interest for the return flow of the Walker cell is depicted in **blue**.

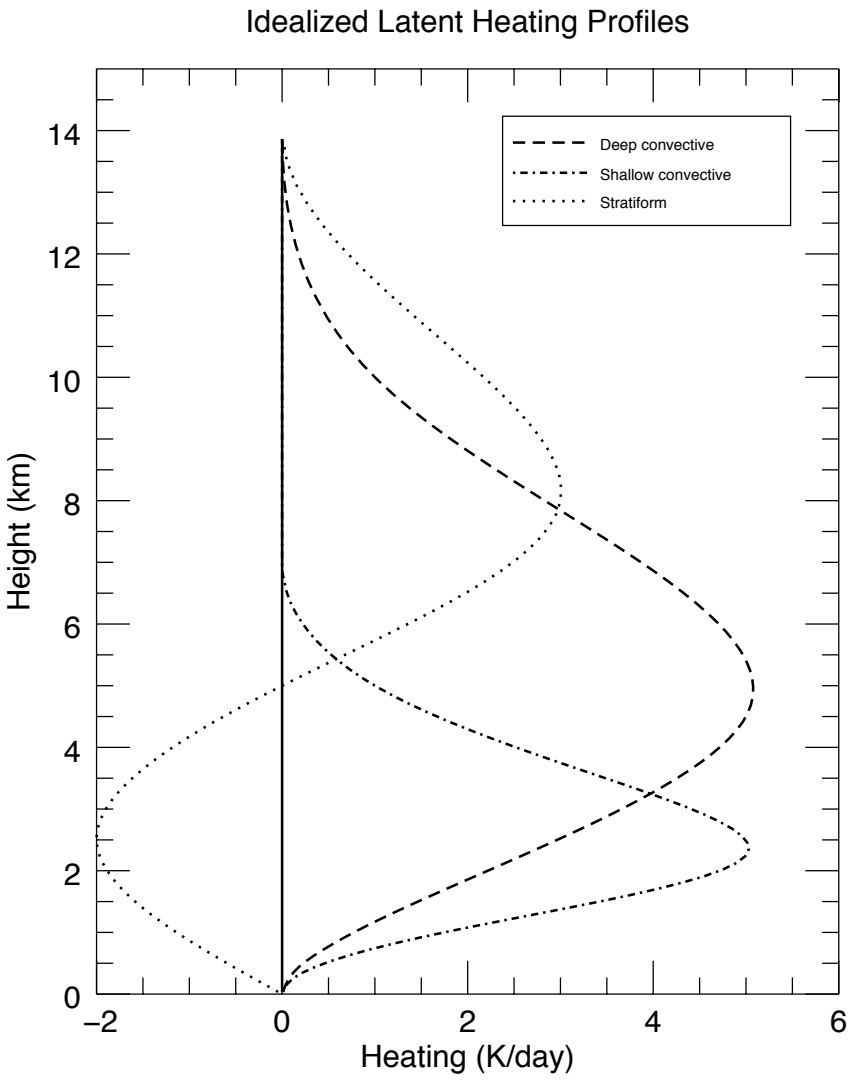

Figure A.4: Idealized latent heating profiles for regions of deep convective, shallow convective, and stratiform rain. From Schumacher et al. (2004).

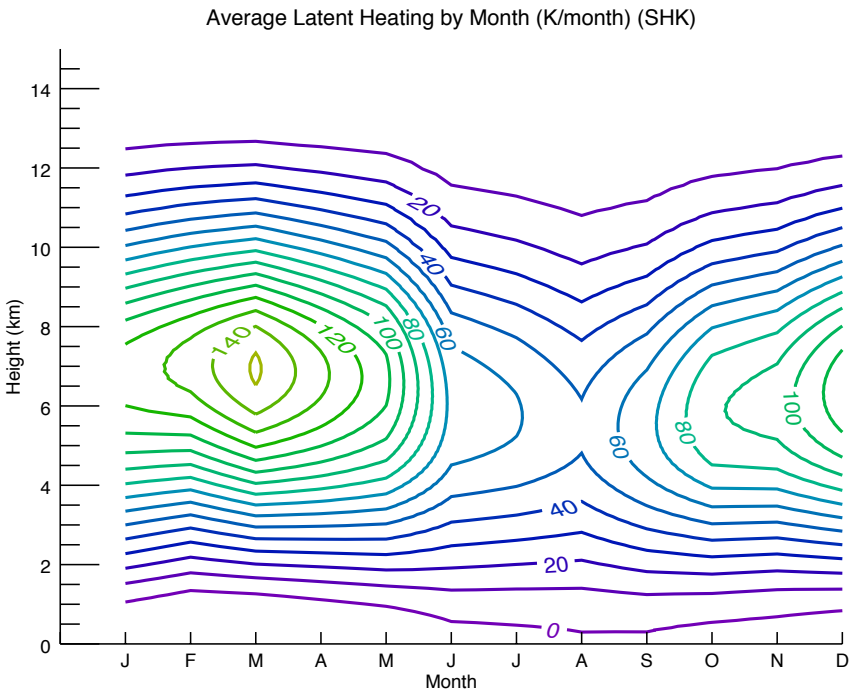

Figure A.5: Contoured latent heating for the Amazon area of interest, as calculated using the TRMM-based SHK method.

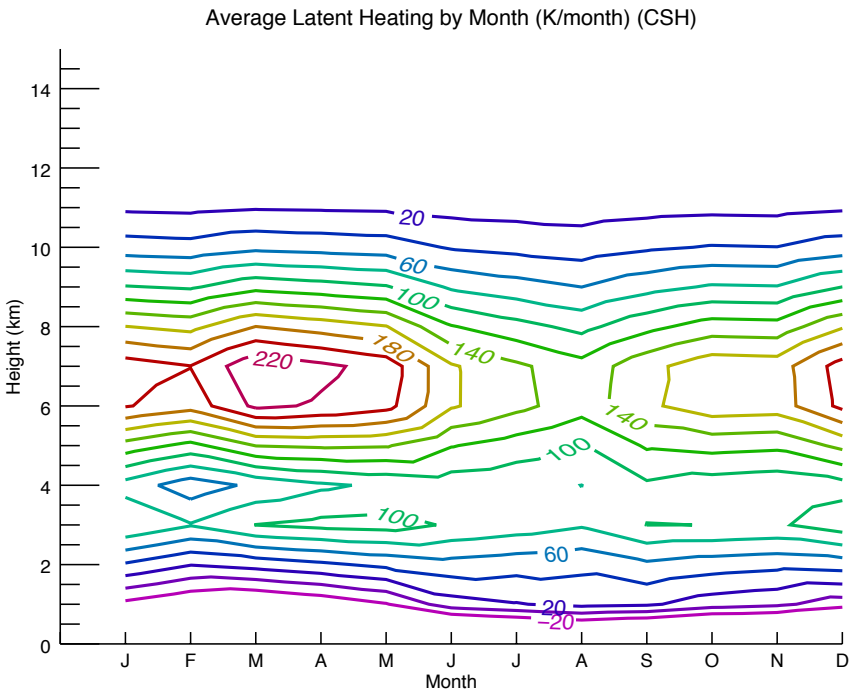

Figure A.6: Contoured latent heating for the Amazon area of interest, as calculated using the TRMM-based CSH method.

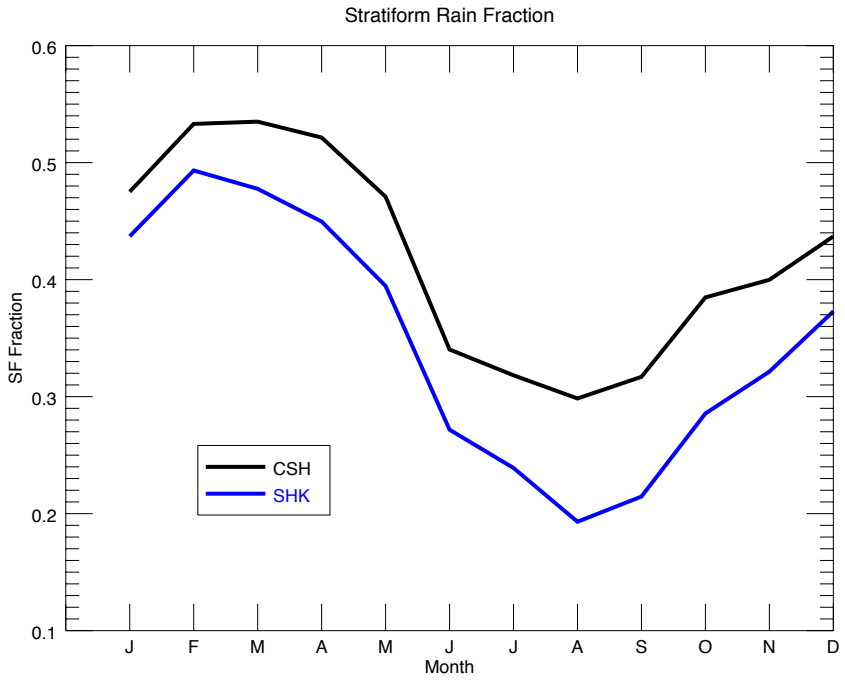

Figure A.7: TRMM PR monthly stratiform rain fractions used as inputs for SHK and CSH over the Amazon domain.

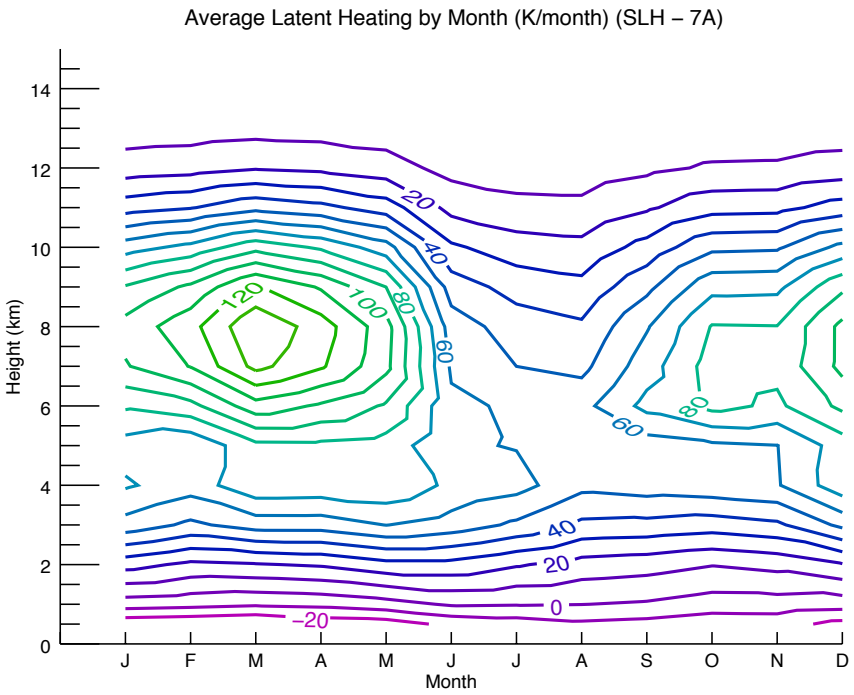

Figure A.8: Contoured latent heating for the Amazon area of interest, as calculated using the TRMM-based SLH method.

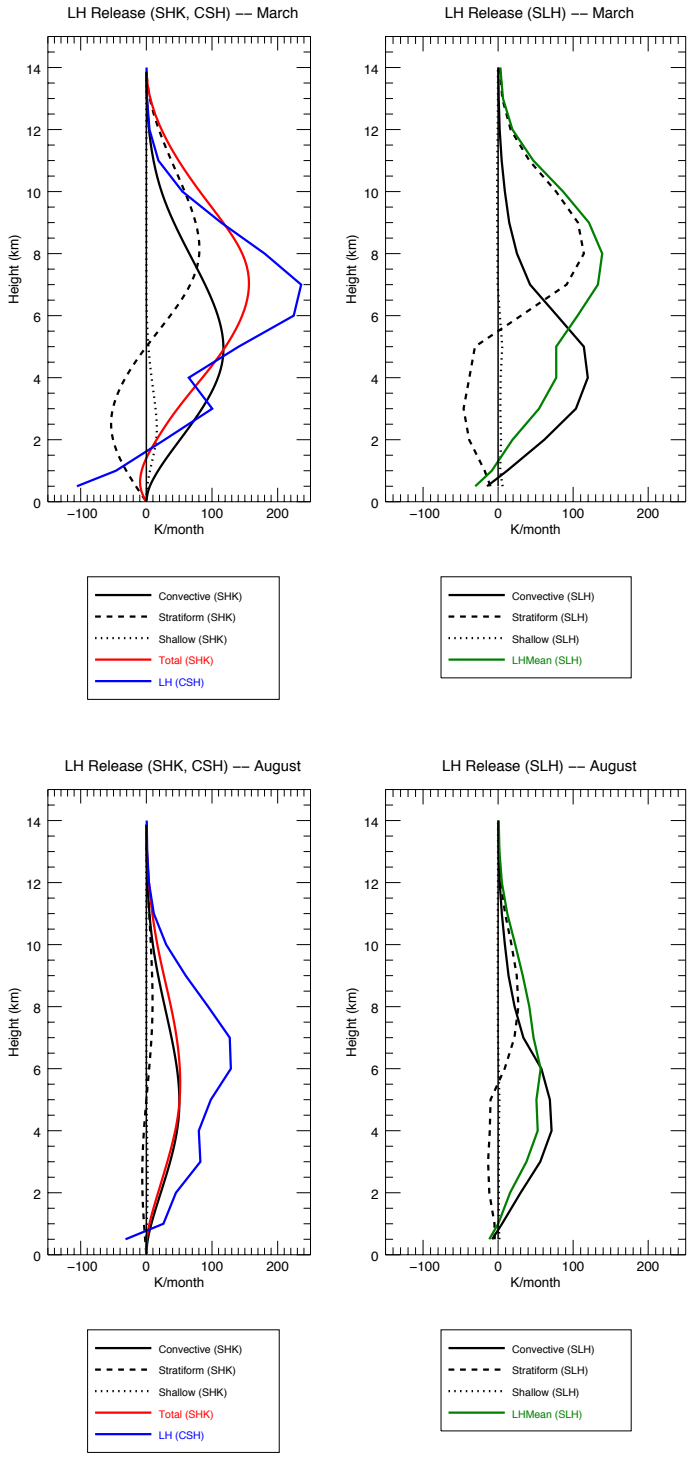

Figure A.9: Latent heating profiles for SHK and CSH (left panels) and SLH (right panels) for March (wet season; top panels) and August (dry season; bottom panels).

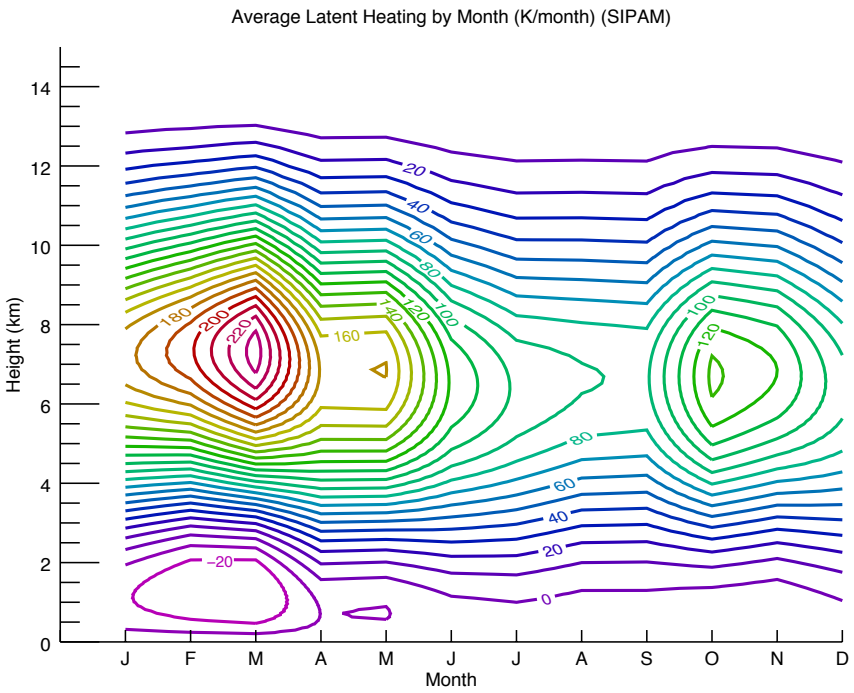

Figure A.10: Contoured latent heating for 110 km radius region around SIPAM radar, as calculated using the SHK method for surface rain rates captured during 2014.

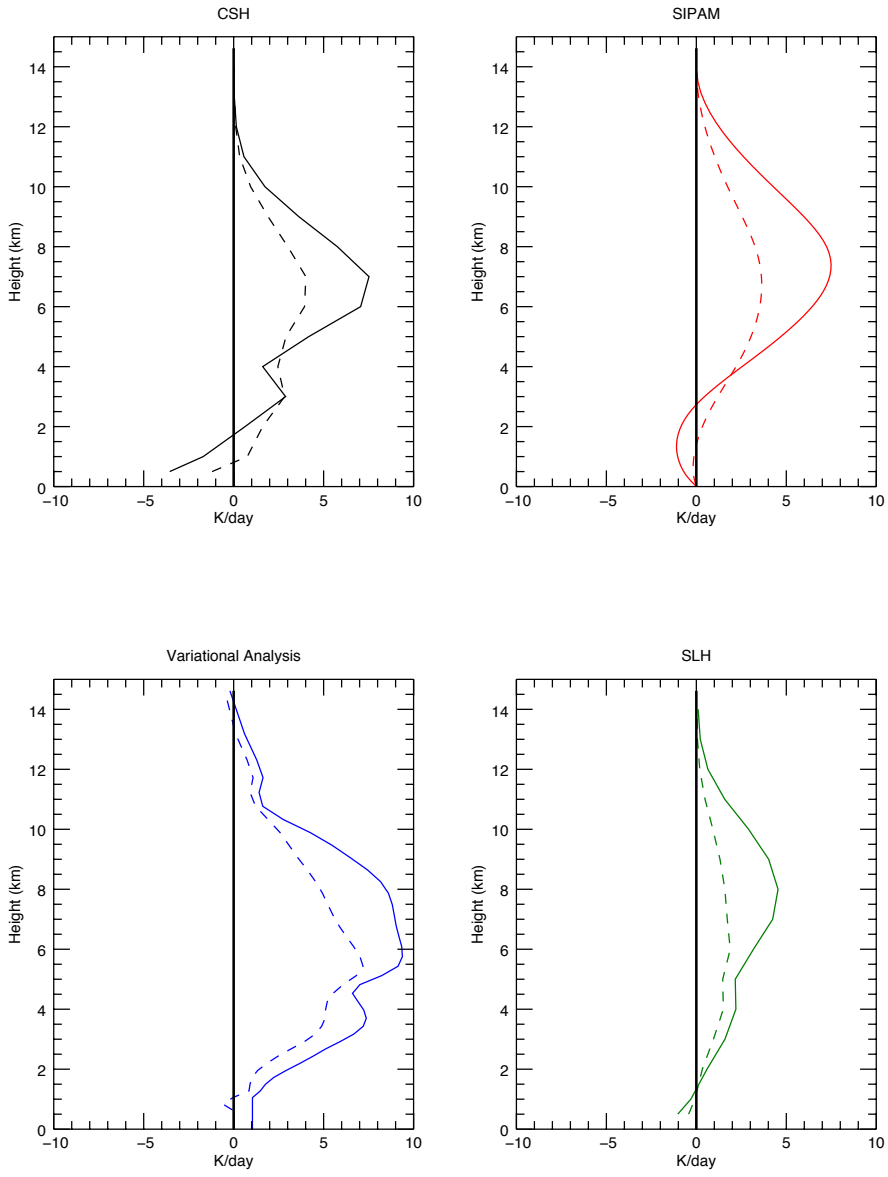

Figure A.11: Vertical profiles during IOP1 (solid lines) and IOP2 (dashed lines) of latent heating averaged across the Amazon spatial domain for CSH, SIPAM, Variational Analysis ($> 0.2mmhr^{-1}$), and SLH.

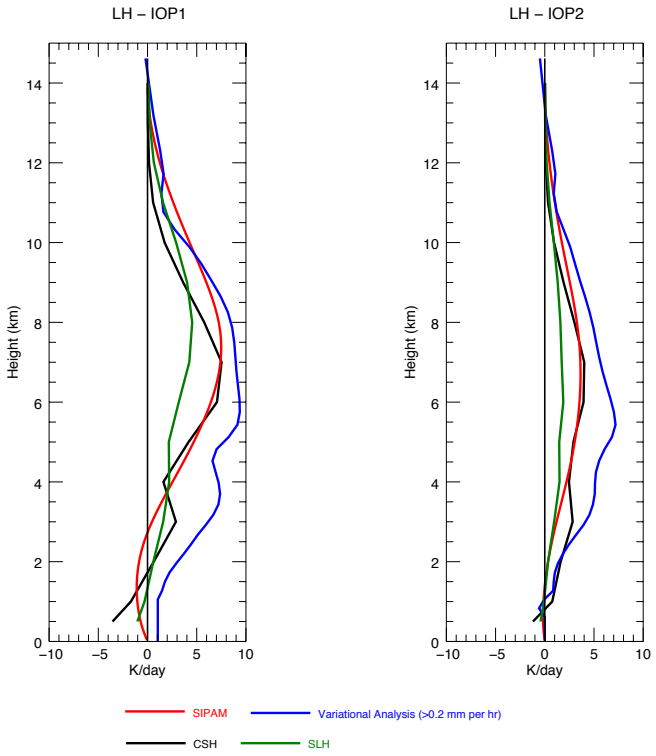

Figure A.12: Vertical profiles of latent heating averaged across the Amazon spatial domain for IOP1 (Feb/Mar 2014; left) and IOP2 (Sept/Oct 2014; right). SIPAM (red), Variational Analysis ($> 0.2mmhr^{-1}$; blue), CSH (black), and SLH (green) are shown.

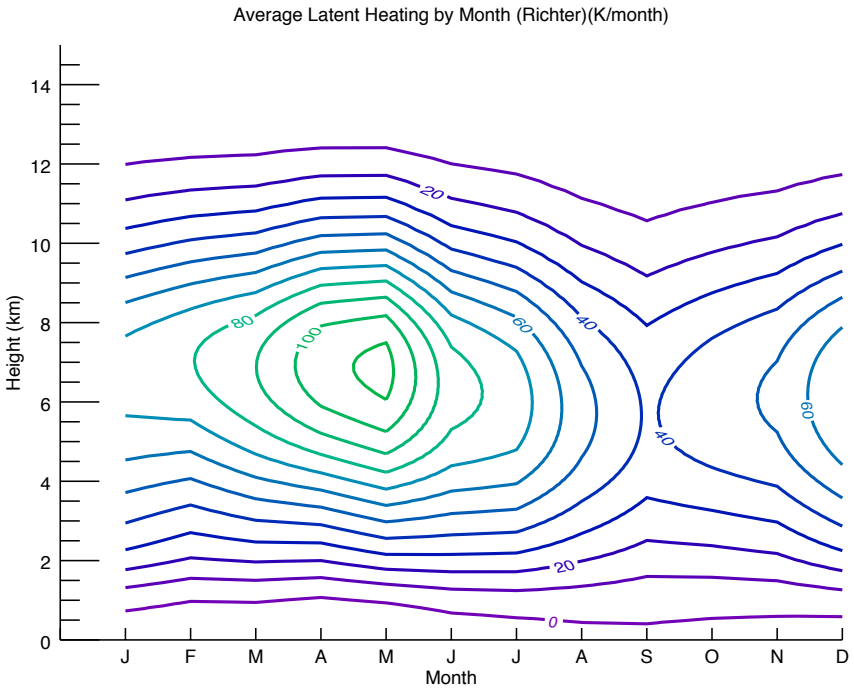

Figure A.13: Contoured latent heating for the Richter and Xie area of interest, as calculated using the TRMM-based SHK method.

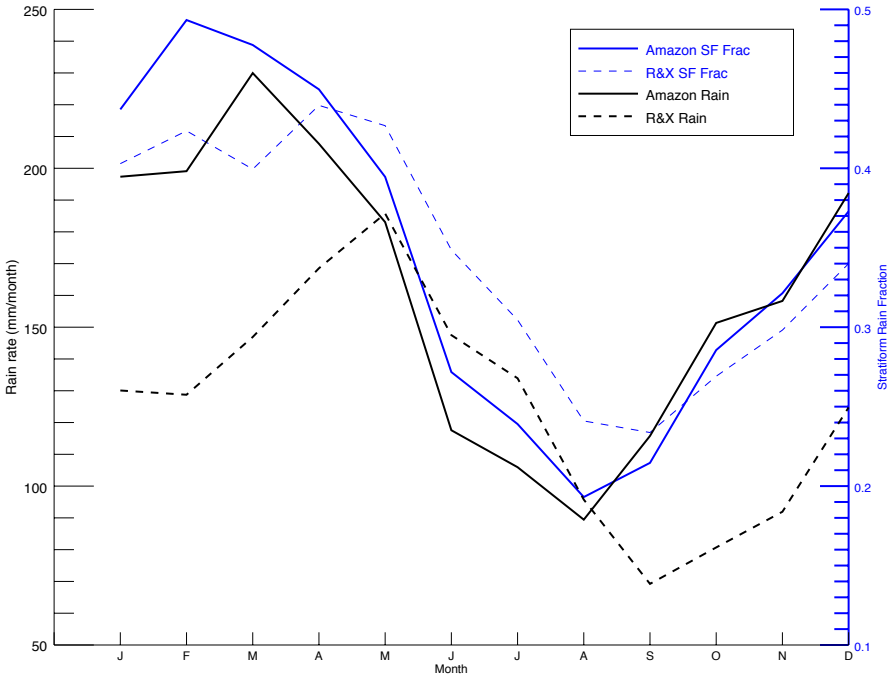

Figure A.14: Climatologies for rain rates (black) and stratiform rain fraction (blue) for the Amazon area of interest (solid line) and the Richter and Xie area of interest (dashed line).

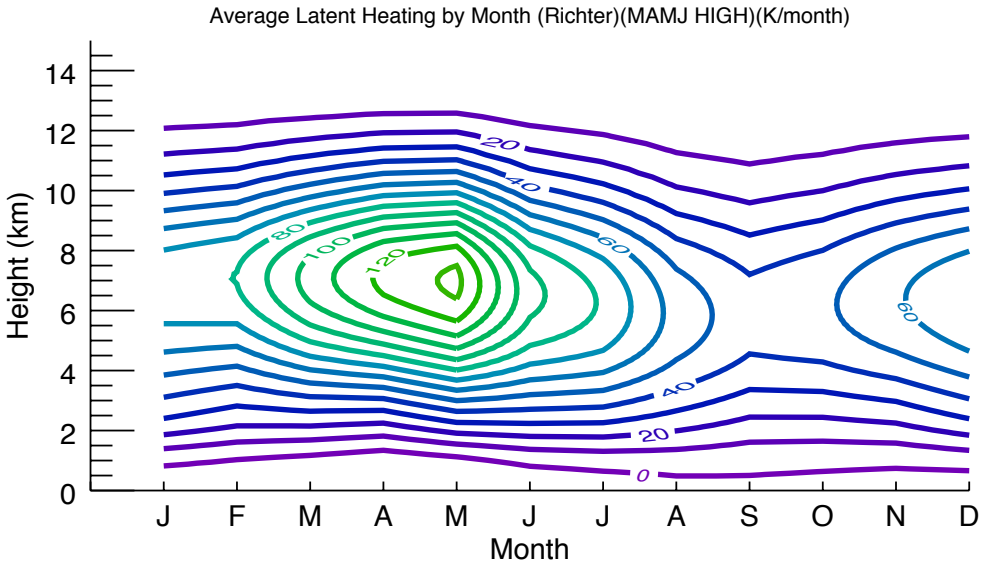

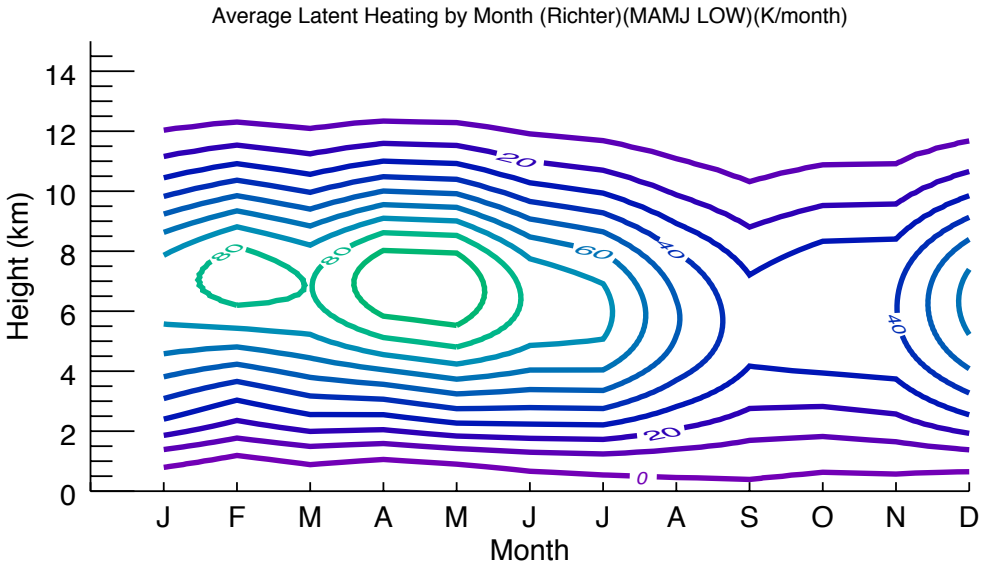

Figure A.15: Contoured latent heating using the group of high years (top panel) and group of low years (bottom panel) for the Richter and Xie area of interest, as calculated using the TRMM-based SHK method.

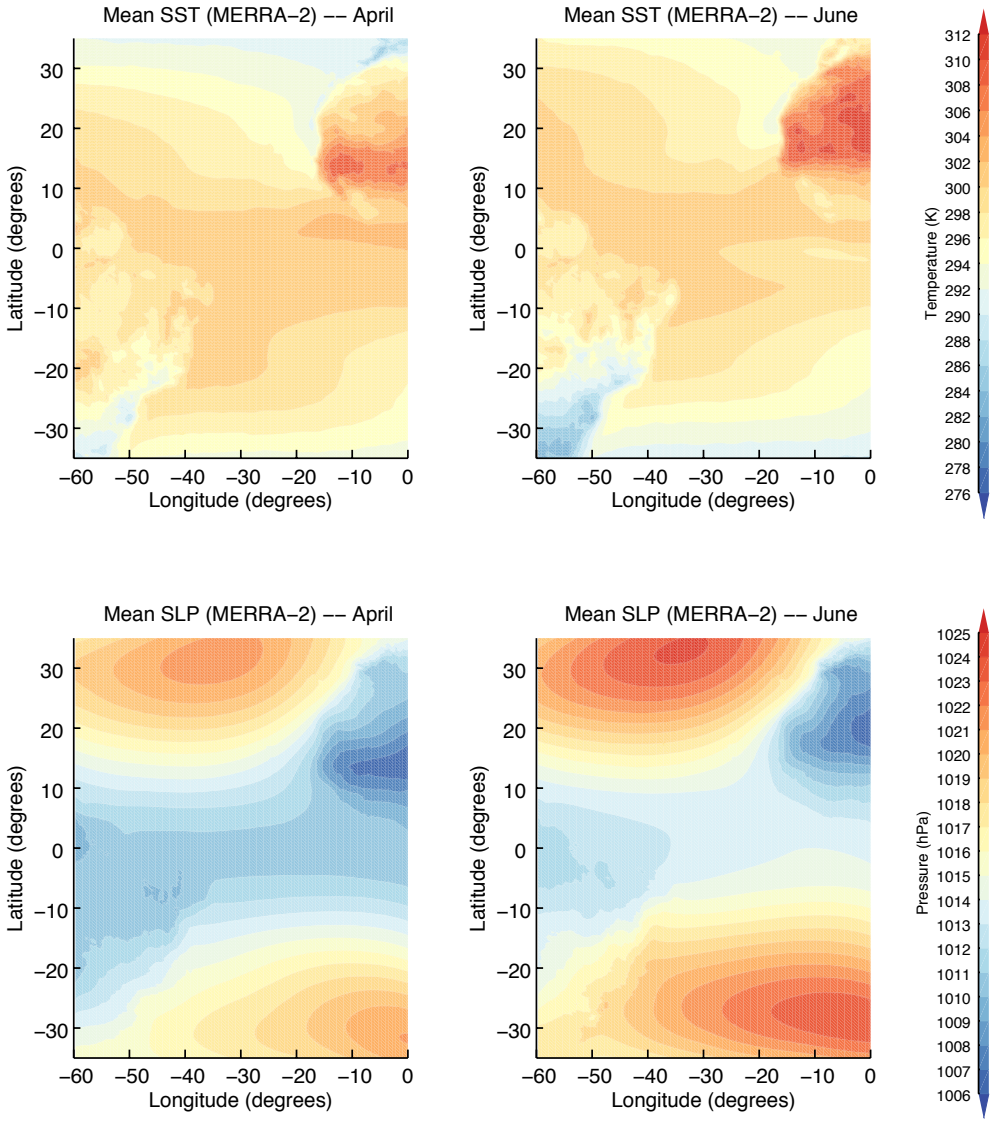

Figure A.16: Climatological averages for SST (top) and SLP (bottom) in April (left) and June (right) using MERRA-2 data.

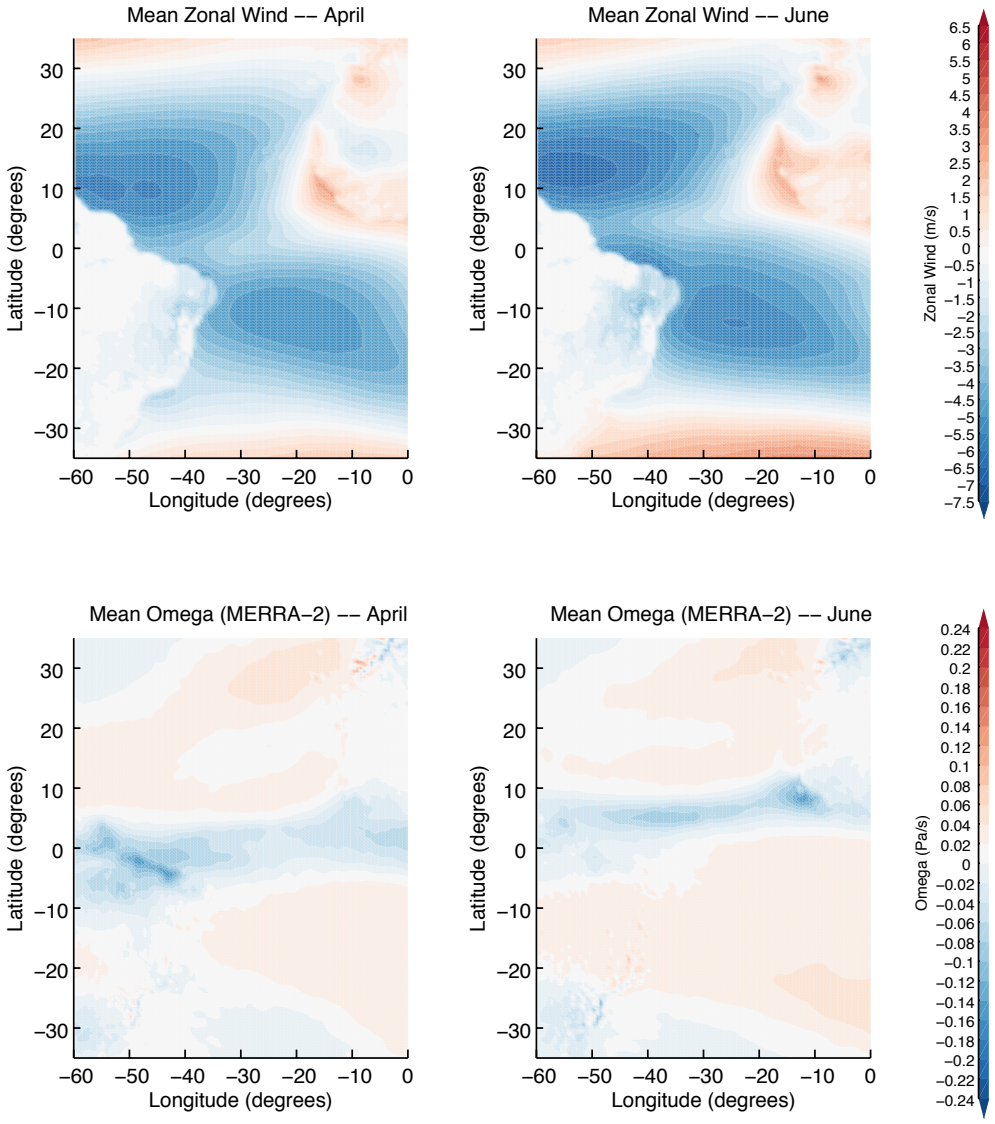

Figure A.17: Climatological averages for zonal wind (top) and 500-hPa omega (bottom) in April (left) and June (right) using MERRA-2 data.

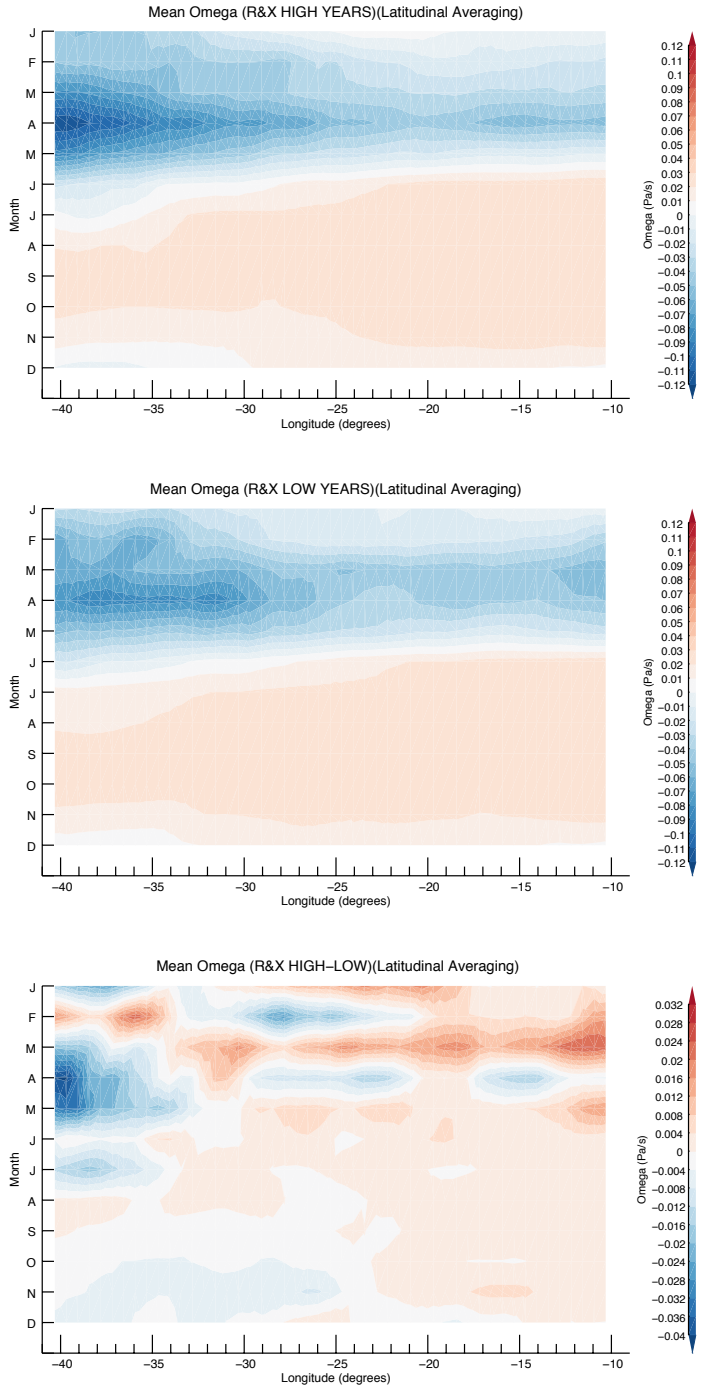

Figure A.18: Contoured omega using the group of high years (top panel), low years (middle panel) and difference (high - low; bottom panel) for the tropical Atlantic.

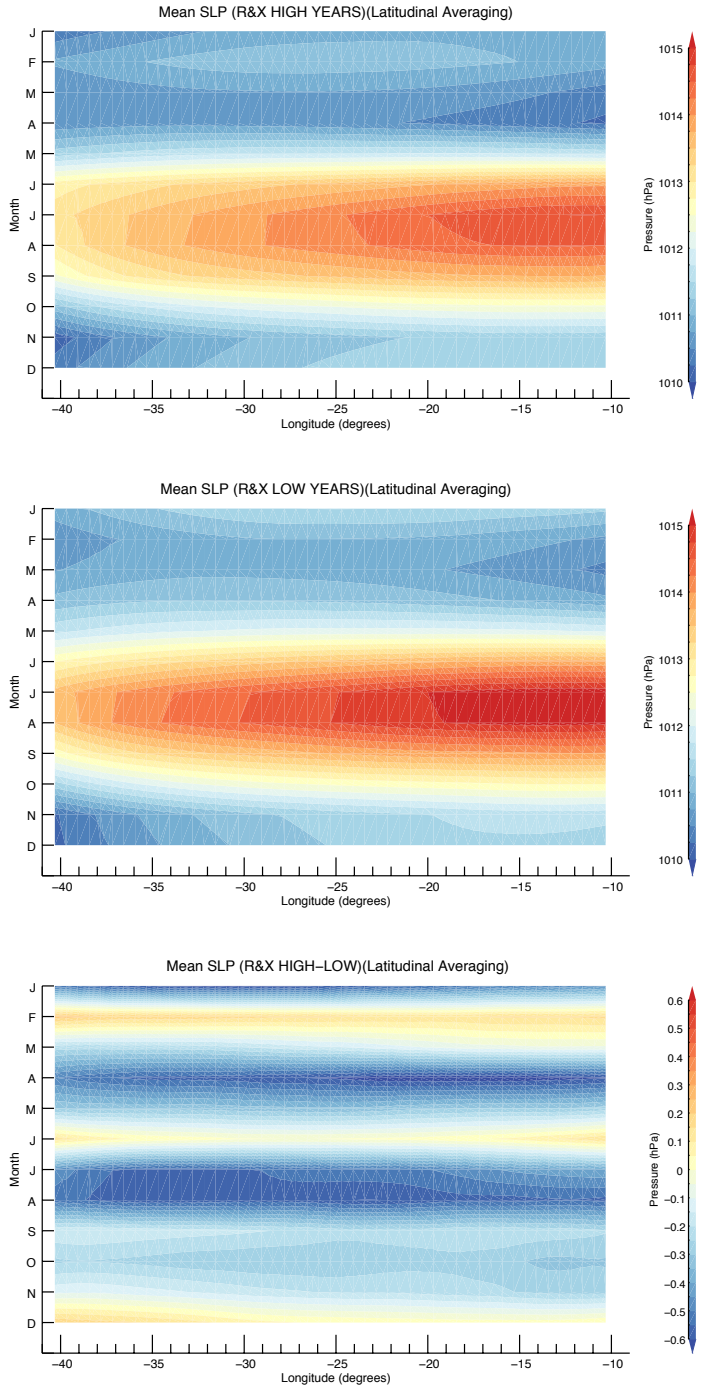

Figure A.19: Contoured SLP using the group of high years (top panel), low years (middle panel) and difference (high - low; bottom panel) for the tropical Atlantic.

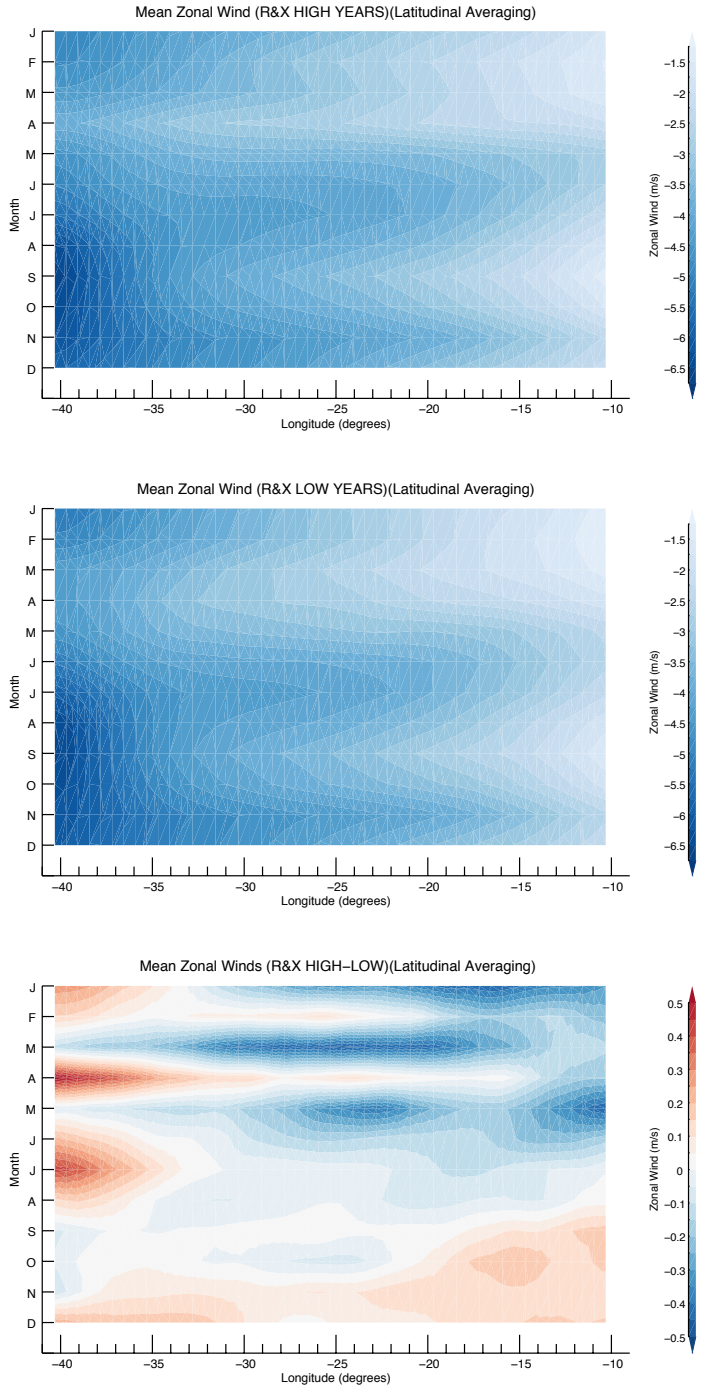

Figure A.20: Contoured zonal winds using the group of high years (top panel), low years (middle panel) and difference (high - low; bottom panel) for the tropical Atlantic.

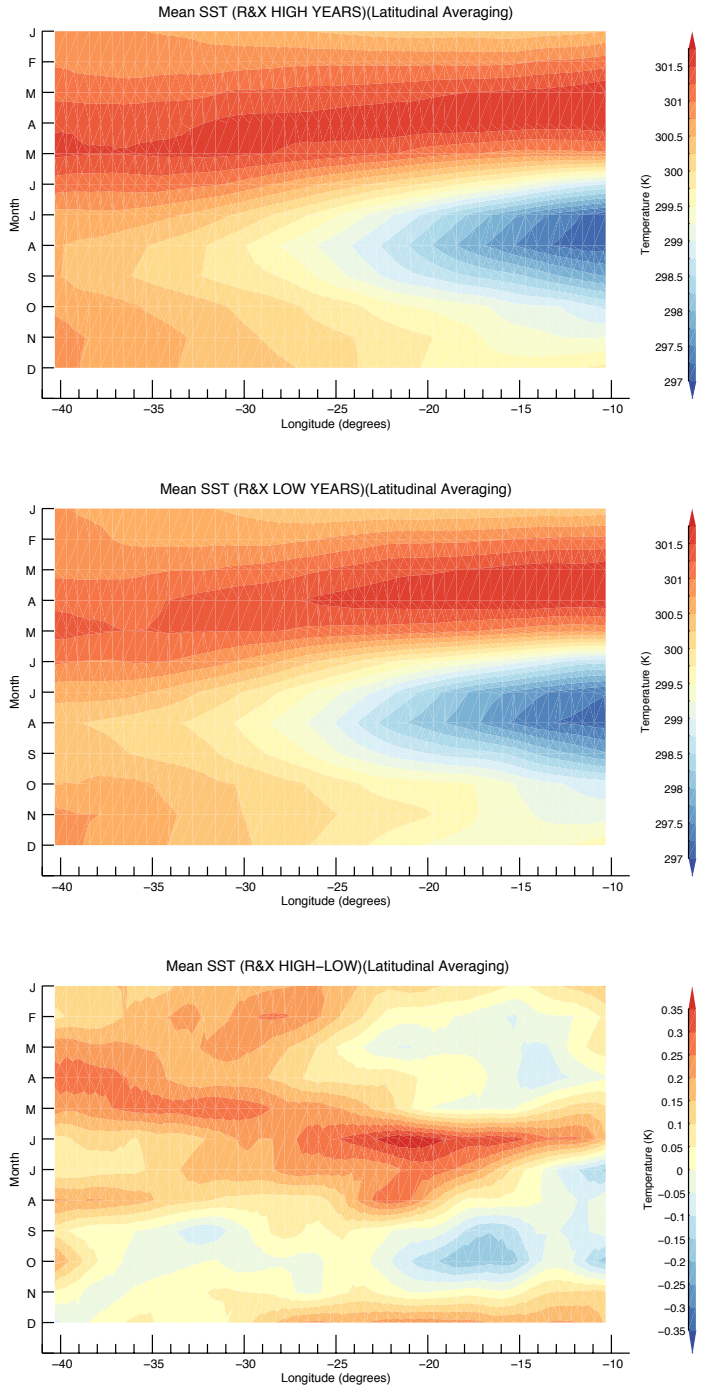

Figure A.21: Contoured SST using the group of high years (top panel), low years (middle panel) and difference (high - low; bottom panel) for the tropical Atlantic.

APPENDIX B

TABLES

Table B.1: Years classified as experiencing relatively higher or lower latent heat release through the 6-8 km layer during the MAMJ wet season.

HIGH	2000, 2002, 2004, 2006, 2007, 2008, 2010, 2011, 2013
LOW	1998, 1999, 2001, 2003, 2005, 2009, 2012, 2014